

Medium- and High-Entropy Spinel Ferrite Nanoparticles via Low-Temperature Synthesis for the Oxygen Evolution Reaction

Judith Zander, Julia Petra Wölfel, Morten Weiss, Yiqun Jiang, Ningyan Cheng, Siyuan Zhang, and Roland Marschall*

High-entropy oxides are a material class that is currently receiving rapidly increasing attention due to the large variety in composition and the adjustable properties. Cooperative effects between different metal cations in the crystal structure in addition to entropic phase stabilization have proven beneficial for electrocatalytic applications. Most synthesis methods, however, require high synthesis temperatures and long times, and additionally only yield selected samples in good phase-purity. Furthermore, toxic or scarce elements are often present in large amounts. Herein, a non-aqueous microwave-assisted solvothermal synthesis is presented as a fast and low-temperature alternative for the fabrication of a wide range of earth-abundant ferrites (AFe_2O_4). Directly crystalline, phase-pure spinel ferrites of various compositions ranging from one to seven different A-ions are successfully obtained after only 30 min at 225 °C. A detailed characterization of their properties in relation to their composition is performed, and they are also employed for the alkaline oxygen evolution reaction. A partial replacement of Fe by Co moreover shows the high versatility of the synthesis that also allows for the simultaneous variation of the B-ion.

the large compositional variety that can be adjusted to tailor target properties.^[14] High-entropy oxides (HEOs) of different crystal structures are known. The elements commonly included depend on the structure type, with Co, Cu, Mg, Ni, Zn, Mn, and Cr frequently featured in rock-salt,^[5,15] or spinel-type HEOs,^[7,6,16,17] whereas fluorite and perovskite HEOs often contain rare-earth metals.^[18–22]

An important parameter in high-entropy materials is the entropic stabilization of the crystal structure since the free energy of mixing (ΔG_{mix}) decreases with an increasing entropy of mixing (ΔS_{mix}).

$$\Delta G_{\text{mix}} = \Delta H_{\text{mix}} - T\Delta S_{\text{mix}} \quad (1)$$

Thermodynamically, the structure can be stabilized if the entropy is high enough to overcome the mixing enthalpy and result in an overall negative ΔG of formation. The entropy in turn increases with an

increasing number of different ions (in this case cations) in the structure. It is furthermore dependent on the mole-fraction and is the highest for equal molar ratios.^[4,23] According to the definition first introduced for alloys, materials can be classified as “high-entropy” if more than five different elements are present in concentrations above 5% for alloys,^[24] or more than five cations for oxides, since the anion fraction is kept constant.^[14,23] In this case the configurational entropy (S_{config}) equals to or exceeds 1.5 R (with R being the gas constant) – at least for alloys.^[24,25] For oxides the situation is more complex, since more than one sublattice is present, and a variation of only the cation contribution will not be enough to exceed a S_{config} of 1.5 R. The contribution of each ion in the oxide depends on the molar fraction and the number of different ions on one site and is approx. zero for oxygen.^[23] Thus, the entropic contribution to ΔG increases with an increasing M/O ratio and the number of different ions on each site.^[26] For more than one cationic sublattice, the situation is even more complex, as the overall configuration entropy not only depends on the number of cations but also on the distribution over the different sites.^[26] From Equation (1) it is additionally obvious, that the formation of high-entropy materials is favored at high temperatures, resulting in commonly high synthesis temperatures, which is impedimental for nanoparticle synthesis.^[23,26]

1. Introduction

Research on high-entropy materials, initially alloys,^[1–4] but later on other material classes such as oxides,^[5–8] nitrides,^[9] or sulphides,^[10–13] boomed in recent years. This is mainly due to

J. Zander, J. P. Wölfel, M. Weiss, R. Marschall
Department of Chemistry
University of Bayreuth
Universitätsstr. 30, 95440 Bayreuth, Germany
E-mail: roland.marschall@uni-bayreuth.de

Y. Jiang, N. Cheng, S. Zhang
Max-Planck-Institut für Eisenforschung
Max-Planck-Str. 1, 40237 Düsseldorf, Germany

 The ORCID identification number(s) for the author(s) of this article can be found under <https://doi.org/10.1002/adfm.202310179>

© 2023 The Authors. Advanced Functional Materials published by Wiley-VCH GmbH. This is an open access article under the terms of the [Creative Commons Attribution](#) License, which permits use, distribution and reproduction in any medium, provided the original work is properly cited.

DOI: 10.1002/adfm.202310179

Additionally, enthalpy-driven phase segregation is a common problem encountered in the synthesis of HEOs, especially at lower temperatures.^[14,27]

The adjustable composition of HEOs is especially interesting for catalytic applications. Adsorption energies and activation barriers are of paramount importance in electrocatalysis, together with synergistic effects between adjacent metal centers – both parameters fundamentally depend on the elemental composition, especially on the surface.^[4,28,13] Due to the large number of different elements in the structure, a large number of different surface atomic sites and chemical environments are available for specific adsorption and activation of reactants. Ideally, it can be adjusted through variations in the composition.^[29] High entropy alloys have been explored as stable electrocatalysts for the hydrogen evolution reaction (HER), oxygen evolution reaction (OER) and oxygen reduction reaction (ORR) alike. By adjusting the elemental composition and thus electronic and surface properties, even multifunctional catalysts are attainable.^[1,4] Apart from noble metals, oxides are frequently employed as electrocatalysts, especially in the field of earth-abundant electrocatalysis. Low overpotentials and good electrochemical stability were reported for HEOs in OER.^[19,30–32] Conductivity and stability against corrosion and cycling are equally important, especially for application in batteries. Entropic stabilization was shown to have a significant influence on capacity retention in HEO electrodes for Li-ion batteries that were much higher compared to their medium-entropy counterparts.^[33]

Spinel oxides of the general formula AB_2O_4 are an interesting class of metal oxides, in which oxygen forms a cubic close-packed lattice, the A-ions occupy 1/8th of the tetrahedral sites and the B-ions occupy half of the octahedral sites. They also exhibit interesting magnetic, electronic, and optical properties that depend on the composition, but also on the cation distribution, described by the degree of inversion.^[34,6] Many spinel oxides have shown promise in electrochemical OER.^[35–40] Most of the reported spinel electrocatalysts contain either iron or cobalt as the cation on the B-site. Compared to cobalt, iron is by far the more abundant, less toxic, and cheaper option. Of the ferrites used for the OER, especially high activities were observed for $NiFe_2O_4$ ^[41–43] and $CoFe_2O_4$.^[44–46] The use of Fe as B-cation additionally allows for an exploitation of the synergy between Ni and Fe.^[47]

An additional interesting property of spinel oxides is the deviation from a normal cation distribution by partial or even complete inversion, in which case A-ions occupy octahedral sites that are exclusively occupied by B-ions in a normal structure and B-ions occupy tetrahedral sites.^[34] This does not only affect the physical properties but also the degree of entropy in the system, as the contribution from B-site-occupation is no longer zero.^[23] The degree of inversion not only depends on the ionic radii of employed cations, the ligand field stabilization energy (LFSE) in tetrahedral and octahedral crystal field, respectively, but also to a large extent on the synthesis strategy.^[48–50] While this introduces another parameter for tailoring the properties via the adjustment of the structure, it makes a prediction of entropic stabilization effects highly challenging.

We have previously reported on the synthesis of several spinel oxides, namely $NiFe_2O_4$,^[42] $MgFe_2O_4$,^[51] and $ZnFe_2O_4$,^[49] the synthesis of which is essentially an adaptation of the non-

aqueous microwave synthesis of metal oxides reported by the group of Niederberger, employing metal acetylacetonates (acac) and an aromatic alcohol derivate.^[52,53] Based on these syntheses that proceed under highly similar reaction conditions, we now herein delineate the versatility of this approach by introducing more than one $M(acac)_2$ precursor into the synthesis. A wide range of phase-pure earth-abundant spinel ferrites (AFe_2O_4) with compositions ranging from one to seven different A-ions could successfully be prepared via this approach at a synthesis temperature of only 225 °C. All of these medium and high entropy oxides were obtained as nanocrystalline powders, with crystallite sizes of ≈ 10 nm. Since the crystallinity generally decreased with an increasing number of different A-ions, subsequent heat-treatment at 400 °C in air could increase the crystallinity without having a negative impact on phase-purity. A detailed characterization of their properties in relation to their composition was performed, and they were also employed for the alkaline oxygen evolution reaction (OER). A partial replacement of Fe by Co moreover shows the high versatility of the synthesis that also allows for the simultaneous variation of the B-ion.

2. Results and Discussion

For the synthesis, the amount of $Fe(acac)_3$ and the total amount of M^{2+} -precursors were kept constant with a targeted yield of 1 mmol MFe_2O_4 per synthesis. Phase-pure ferrites of Co, Mn, Mg, Zn, and Ni were obtained in agreement to previously reported results.^[42,54] While the crystallinity of $NiFe_2O_4$ directly after the microwave-assisted synthesis is low and $MgFe_2O_4$ is not yet fully condensed, subsequent calcination at 400 °C yields phase-pure, nanocrystalline ferrites with all different A-ions (Figure S1, Supporting Information). In the next step, ternary oxides were synthesized, containing two of these M^{2+} -ions in equal amounts. Phase-pure ferrites could be obtained for different combinations of Co, Mn, Mg, Zn, and Ni. Only the addition of Cu as a second A-ion resulted in phase-separation, due to a reduction of copper (Figure S2, Supporting Information), especially if Zn and Mg are used as second M^{2+} -ion.

Since $NiFe_2O_4$ has shown promise as an efficient electrocatalyst for the OER, before,^[42,41] Ni was also included in the synthesis of more complex spinel oxides. The ratio of Ni-precursor was progressively lowered, as Ni^{2+} was partially replaced by more and more different M^{2+} -precursors. All M^{2+} -ions were employed in equal ratios. Spinel ferrites with three up to seven different M^{2+} -ions could successfully be obtained, thus reaching compositions that can be considered as “high-entropy” based on the definition of more than five different cations in a sublattice, although true entropic-stabilization is not verified (Figure 1; Figures S3–S6, Supporting Information). Interestingly, the inclusion of Cu is possible for spinels with four or more different M^{2+} -ions, although phase-separation was observed for the ternary oxides. This could be an indication of entropic stabilization. The obtained ferrites $(NiCuCoMn)Fe_2O_4$ and $(NiCuCoZn)Fe_2O_4$ appear completely phase-pure when characterized with Cu-X-ray diffraction (XRD). Very small reflections for Cu are observed when zooming in on the high-resolution Ag-XRD patterns, which might be an indication that entropic stabilization is not yet entirely sufficient for these oxides. No by-phases are observed after heat-treatment at 400 °C, which supports the assumption

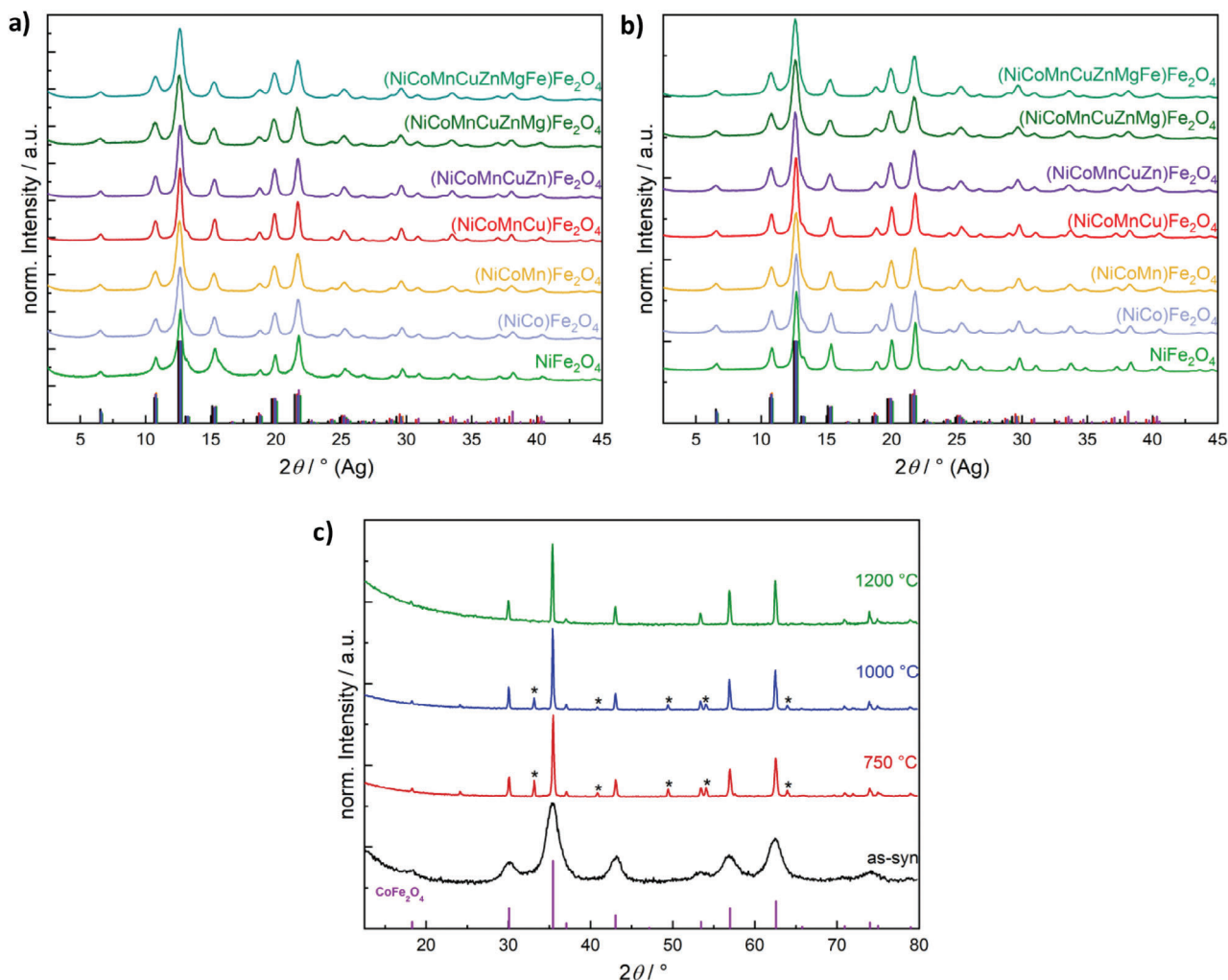


Figure 1. High-resolution Ag-XRD patterns of medium and high-entropy oxides prepared based on the synthesis of NiFe_2O_4 with introduction of progressively more M^{2+} ions into the synthesis: as-synthesized a) and subsequently calcined b). Following ICDD reference cards were used: Co: 00-022-1086; Mn: 01-074-2403; Zn: 00-022-1012; Ni: 01-074-2081; Mg: 01-071-1232. Reversible mixing-demixing upon calcination is demonstrated by the normalized Cu-XRD patterns for $(\text{NiCoMnCuZnMg})\text{Fe}_2\text{O}_4$ in (c). Emerging reflections of Fe_2O_3 upon demixing are marked by an asterisk.

of entropy effects stabilizing the structure, although the presence of trace amounts of CuO cannot be excluded (Figure S4, Supporting Information). The synthesis temperature of 225°C in the microwave is significantly lower, compared to other reported synthesis methods for high-entropy spinel oxides, in which commonly temperatures $\approx 1000^\circ\text{C}$ are required.^[55,6,7] The assumption of entropic stabilization could be further cemented by reversible demixing upon calcination – an experiment well-known for HEOs with a rocksalt structure.^[5] Calcination of as-synthesized $(\text{NiCoMnCuZnMg})\text{Fe}_2\text{O}_4$ at 750°C for 5 h results in a demixing and the appearance of reflections for a Fe_2O_3 side-phase. This transition is driven by enthalpic contributions since the mixing enthalpy favors phase segregation. Subsequent calcination for 5 h each at 1000 and 1200°C progressively leads to a transition back to a phase-pure spinel structure (Figure 1c). This observation is an indication for entropic stabilization of the structure, while at the same time demonstrating that the microwave-assisted approach is able to yield a kinetically-controlled product

that is not the thermodynamically most favored one at the given synthesis temperature of 225°C .

Raman spectroscopy is a useful tool to further evaluate phase-purity, since the shift and intensity of observed vibrational modes depend on the structure, as does the sensitivity to Raman scattering. Thus, highly Raman-active phases might be observable, which may have too low concentrations to appear in powder XRD patterns. Additionally, the characteristic bands for Raman-active vibrations in the spinel structure depend on the degree of inversion, since occupation of one crystal site by more than one different cation will result in a splitting of the observed modes.^[34] Some of the herein-employed M^{2+} -ions favor the inverse spinel structure, as in the case of NiFe_2O_4 , while others, such as ZnFe_2O_4 , almost exclusively occur in the normal spinel structure (Figure 2).^[34]

In many cases, the actual structure is somewhere between the ideally normal and the completely inverted structure. The degree of inversion significantly influences optical and electronic

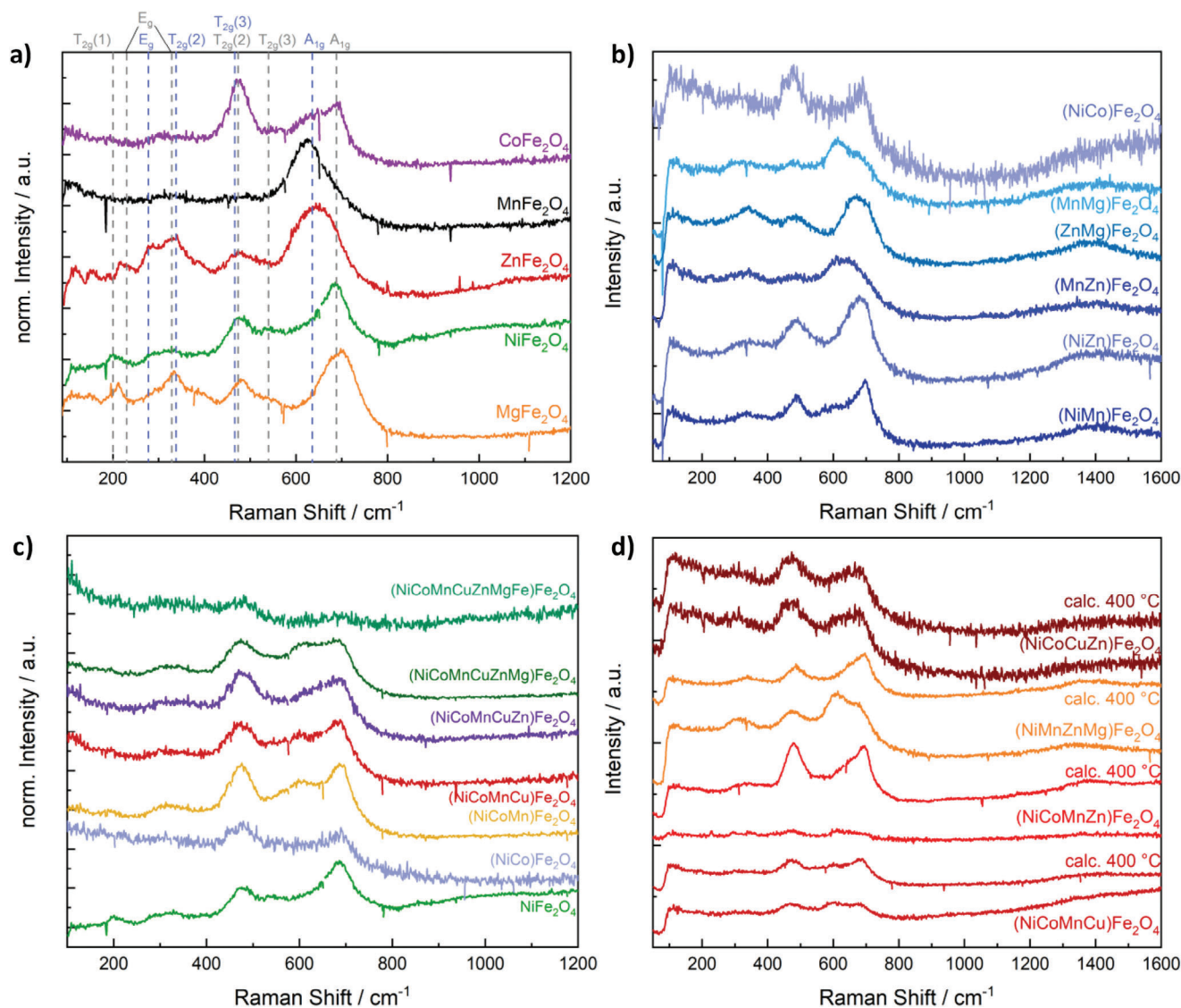


Figure 2. a) Raman measurements for calcined binary ferrites, b) ternary ferrites, and c) ferrites with increasingly more M^{2+} -ions. d) The influence of calcination on the cation distribution is elucidated exemplarily for ferrites containing four different M^{2+} -ions. Approximate positions for a normal spinel structure are shown in blue, those for an inverse structure in grey.^[34]

properties of the material. In the special case of many different metal cations in the system, the possibility for site-exchange with the Fe^{3+} ions also affects the entropy, since a distribution of the M^{2+} -ions over the B-sites significantly increases the configurational entropy, since it is no longer restricted to only one sublattice.^[17] Such an effect has already been reported by Navrotsky et al. in the 1960s for binary spinels, in which partial inversion results in an increase in the configurational entropy that in turn affects the entropy of formation.^[56,57] This can be seen by regarding the equations for configuration entropy in an oxide, not only considering the entropy in one sublattice, as frequently done, but the sum of all lattice contributions together.

In a binary oxide, S_{config} can be calculated as^[23]:

$$S_{\text{config}} = -R \left[x \cdot \left(\sum_{a=1}^M x_a \ln x_a \right)_A + y \cdot \left(\sum_{b=1}^N x_b \ln x_b \right)_B + z \cdot \left(\sum_{o=1}^P x_o \ln x_o \right)_O \right] \quad (2)$$

Assuming an absence of oxygen defects and a spinel structure of AB_2O_4 , this simplifies to:

$$S_{\text{config}} = -R \left[1 \cdot \left(\sum_{a=1}^M x_a \ln x_a \right)_A + 2 \cdot \left(\sum_{b=1}^N x_b \ln x_b \right)_B \right] \quad (3)$$

If the B-site was occupied solely by iron, this would further result in:

$$S_{\text{config}} = -R \left(\sum_{a=1}^M x_a \ln x_a \right)_A \quad (4)$$

If x_b , that is, the relative mole fraction for each different ion on the B-site was no longer 1 – as in the case for only Fe on the B-position – the contribution of the B-sublattice to the

configurational entropy would no longer be zero. Since the preferred site depends on the nature of the ion, the overall configurational entropy does not only depend on the number of different employed ions, but also on their nature. While an accurate determination of the degree of inversion based on Raman measurements is difficult due to small differences in the observed Raman shifts and significant absorption of the incident laser light (red) by the dark-brown ferrites, a qualitative assessment of the cation distribution might be attempted.

Due to the relatively low crystallinity directly after the microwave synthesis, we initially focussed on the spectra of calcined samples. By regarding the $A_{1g}(1)$ and $A_{1g}(2)$ bands between 650 and 700 cm^{-1} and the T_{2g} bands between 600 and 300 cm^{-1} , it can be inferred from the spectra of binary spinels that CoFe_2O_4 , NiFe_2O_4 , and MgFe_2O_4 are mostly inverse, whereas ZnFe_2O_4 and MnFe_2O_4 appear to be mostly normal, in good agreement to literature.^[57,34,58,59] The A_{1g} bands are thereby associated with M–O stretching bonds in tetrahedral sites, whereas the T_{2g} bands arise from asymmetric stretching and bending M–O vibrations at octahedral sites.^[34,59] Occupation of more than one cation at one site results in peak-splitting, since a different cation mass and different M–O bond strength result in a shift of the vibration frequency.^[34] The spectra are fit with Gaussian-Lorentzian peak shapes (GL(50)), assuming one peak for each, A_{1g} , $T_{2g}(3)$, $T_{2g}(2)$, E_g and, if visible, one for $T_{2g}(1)$, each for a normal spinel structure and peak splitting into two modes for the inverted structure, due to tetrahedral and octahedral sites both being occupied by two different ions (Figure S7).^[34] From all samples, MnFe_2O_4 shows the most normal spinel structure, with shoulders between 250 and 400 cm^{-1} , that is, around the region expected for the $T_{2g}(2)$ peak in a normal spinel structure – indicating a low degree of inversion for ZnFe_2O_4 . CoFe_2O_4 is the most inverted spinel, according to the Raman fits, as indicated by the highest $T_{2g}(3)$ to A_{1g} ratio – a similar observation has been made in literature.^[59,60] The same general result is obtained by Rietveld refinement of the Ag-XRD patterns of the binary ferrites (further discussion in the following), which yields a degree of inversion of 0.91 for CoFe_2O_4 , 0.95 for NiFe_2O_4 , and 0.92 for MgFe_2O_4 , while for ZnFe_2O_4 a degree of inversion of 0.32 is obtained. No accurate fit of the cation distribution was possible for calcined MnFe_2O_4 , likely due to the higher amount of amorphous phases that precede decomposition products, alongside the very low degree of inversion and highly similar atomic form factors of Mn and Fe. All values are given after calcination. When adding a second A-ion to the synthesis, still a significant dependence of cation distribution on the nature of the employed ion can be observed (Figure 2). While the spectra of $(\text{NiMn})\text{Fe}_2\text{O}_4$ and $(\text{NiZn})\text{Fe}_2\text{O}_4$ closely resemble that of NiFe_2O_4 for an inverse spinel, those of $(\text{ZnMg})\text{Fe}_2\text{O}_4$ and $(\text{MnZn})\text{Fe}_2\text{O}_4$ are much more similar to that of ZnFe_2O_4 , implying a normal spinel structure, with $(\text{MnMg})\text{Fe}_2\text{O}_4$ lying somewhere in between. This is an indication that Ni has a dominant influence in realizing an inverse spinel structure, whereas Zn pushes for a normal structure. A similar effect was reported by Jadhav et al, who observed a change from a normal towards an inverse spinel structure for $(\text{Ni}_x\text{Zn}_{1-x})\text{Fe}_2\text{O}_4$, with an increasing Ni-ratio.^[61] Generally, the bands are very broad, and even in the Ni-containing compositions, an additional shoulder slightly above 600 cm^{-1} is present. This is due to the fact that even in a normal spinel structure, two different cations now reside on the A-

site, which will always result in a splitting of active modes at least for one site. This fact makes a differentiation between more normal or more inverse structures almost impossible for more extensively substituted compositions. As apparent in Figure 2c, bands become very broad with an increasing number of cations and almost all spectra have a prominent feature between 450 and 500 cm^{-1} , which would correspond to the $T_{2g}(2)$ in an inverted binary spinel. This supports increasing cation disorder – also on the octahedral sites.

Another interesting difference between the spectra is the relative intensity of the $T_{2g}(2)/T_{2g}(3)$ band between 400 and 500 cm^{-1} , which can be attributed to asymmetric bending and stretching of metal-oxygen bonds at octahedral (B)-sites.^[34] The intensity is low for MnFe_2O_4 with Mn^{2+} in d^5 high-spin configuration and especially pronounced in CoFe_2O_4 with Co^{2+} in d^7 configuration, and thus depends on the occupation of d-orbitals with electrons. For Ni^{2+} the intensity is slightly lower again, likely due to an equal distribution of electrons at least over the e_g orbitals. From this observation it can be assumed that samples featuring a high intensity of this T_{2g} band likely contain larger amounts of Co^{2+} and Cu^{2+} on octahedral sites and are thus at least partially inverted. This is the case for almost all compositions shown in Figure 2c. As mentioned above, the partial inversion of the structure increases the disorder in the structure and thus the entropy.

Subsequent calcination increases the crystallinity and thus the intensity of the observed bands (Figure 2d; Figure S7, Supporting Information). Additionally, the relative intensities of the bands change, which is especially prominent for $(\text{NiMnZnMg})\text{Fe}_2\text{O}_4$, for which the spectrum of the as-synthesized sample shows a closer resemblance to that of a normal spinel structure, whereas the one calcined at $400\text{ }^\circ\text{C}$ is very similar to that of an inverted spinel. This could on the one hand be an indication of a change in the cation distribution, which is at first partly determined by kinetics in the synthesis, but on the other hand it could also elucidate the increasing influence of the entropic contribution to ΔG at higher temperatures and underlines an increased stabilization of the inverted structure compared to the normal one.

Now having established macroscopic phase-purity, we wanted to confirm the uniform distribution of the elements in the structure. We performed scanning electron microscopy (SEM) and energy dispersive X-ray spectroscopy (EDX) analysis of various samples (as-synthesized), including elemental mapping for several spinel ferrites with four or more different M^{2+} -ions employed in the synthesis. All of the synthesized ferrites are nanoparticles that form larger agglomerates (Figure 3; Figures S8–S13, Supporting Information).

A slight decrease in the particle diameter from slightly above 20 nm for $(\text{NiCo})\text{Fe}_2\text{O}_4$, down to 15–20 nm in the four M^{2+} -ions containing spinel $(\text{NiCoMnCu})\text{Fe}_2\text{O}_4$ to ≈ 10 nm in the six M^{2+} -ions containing $(\text{NiCoMnZnMgFe})\text{Fe}_2\text{O}_4$ is observable, but the size is very small in all cases. The relative element ratios were determined by analyzing at least two different point areas and are listed in Table S1 (Supporting Information). The relative ratios of the employed M^{2+} -ions are in all cases highly similar. Only the concentration of Mg seems to be a little lower, which is in agreement to previous results for MgFe_2O_4 , in which the employed Mg was not completely incorporated into the structure.^[51] In some cases, the concentration of Cu appears to be a little higher compared to that of the other M^{2+} -elements. This might,

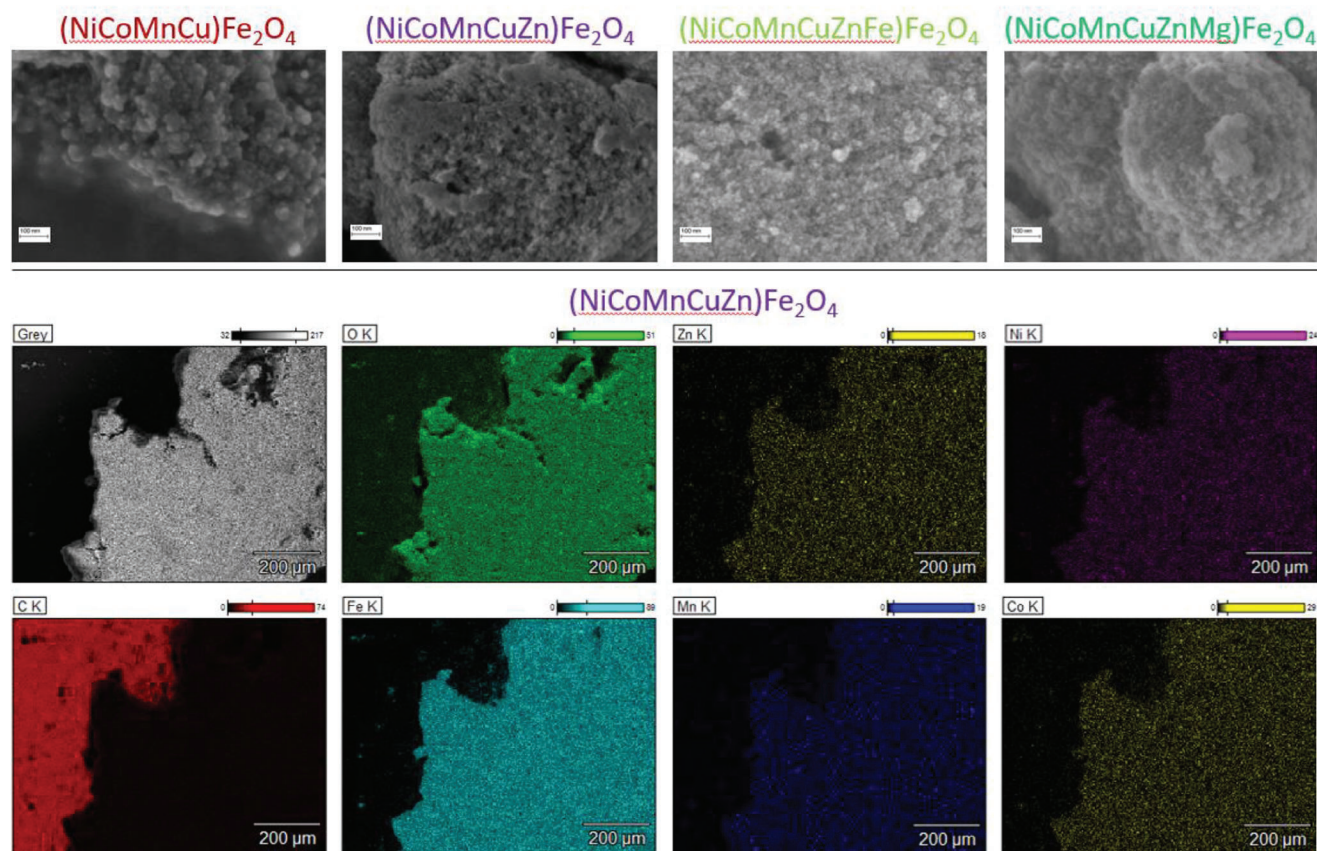


Figure 3. SEM images of four exemplary spinel ferrites with 4 to 7 different M^{2+} ion and EDX mapping of $(\text{NiCoMnCuZn})\text{Fe}_2\text{O}_4$, elucidating the homogeneous distribution of all elements in the structure.

however, be partially an effect of overlap of the Cu-K_α peak with the Pt-L_α peak. Pt was used as a coating in the sample preparation to prevent charging effects. The M^{2+}/Fe ratio is between 0.4 and 0.5 for most samples, independent of the number of employed M^{2+} -ions. This is slightly lower than the ideal ratio of 0.5. A major problem in the quantification of elements is the rather similar energy of the respective K_α -irradiation, which results in an overlap of peaks in the EDX due to insufficient resolution. This results in significant uncertainties in the absolute contributions, especially for combinations of Co and Ni, or worse for Co and Fe. In the latter case, it is especially difficult to distinguish between the Co K_α and Fe K_β lines. In the EDX maps of all ferrites with four or more different M^{2+} -ions, a homogeneous distribution of the elements over the entirety of the analyzed area is observed (Figure 3, Figures S8–S13, Supporting Information). However, to eliminate any doubts about the apparent distribution due to peak overlap, we performed wavelength dispersive X-ray spectroscopy (WDX) analysis for $(\text{NiCoMnCuZnMg})\text{Fe}_2\text{O}_4$. This allows for an accurate separation between the Co K_α and Fe K_β line (Figure S14, Supporting Information).

X-ray photoelectron spectroscopy (XPS) survey scans of spinel ferrites with different compositions confirm the presence of all employed elements, not only in the bulk, but also on the surface (Figure 4; Figure S15, Supporting Information), which is important for, for example, catalytic applications, in which reagent adsorption, activation and conversion are all surface mediated pro-

cesses. An accurate quantification of the elements present is difficult since a strong overlap with often more than one Auger signal is unavoidable when several transition metals are present in the structure. This, together with low concentrations and organic residues from the synthesis, seriously interferes with quantification attempts. Additionally, the Mg 1s and Mg 2s signals were so weak as to be hardly visible at low concentrations. Therefore, the Mg KLL line at 302 eV was used for quantification. Additionally, we measured high-resolution scans from 30 to 150 eV, which allows for a reasonable resolution of the $M 3p$ and $3s$ peaks. These we used for the quantification since they do not overlap with Auger lines and in addition to that can be fitted with one peak instead of complex multiplets. Exemplary fits are shown in Figure 4c. The quantification results are summarized in Table S2 (Supporting Information). While the A/Fe ratio is ≈ 0.5 for most samples, some deviate considerably. This is most likely due to the low intensity of the $M 3s$ and $3p$ peaks, possible uncertainties in the relative sensitivity factors (RSFs) for these rarely used signals and significant peak overlap. The M/O ratio is significantly lower than the ideal value of 0.75, probably due to large amounts of organic residues in the as-synthesized samples. Therefore, the XPS results have to be solely seen as a qualitative evaluation of the composition.

Using alcohols as a solvent, redox-reactions can occur during the synthesis.^[53] M^{2+} -ions might be further oxidized or reduced, while M^{3+} -ions, in this case Fe^{3+} , could be partially reduced,

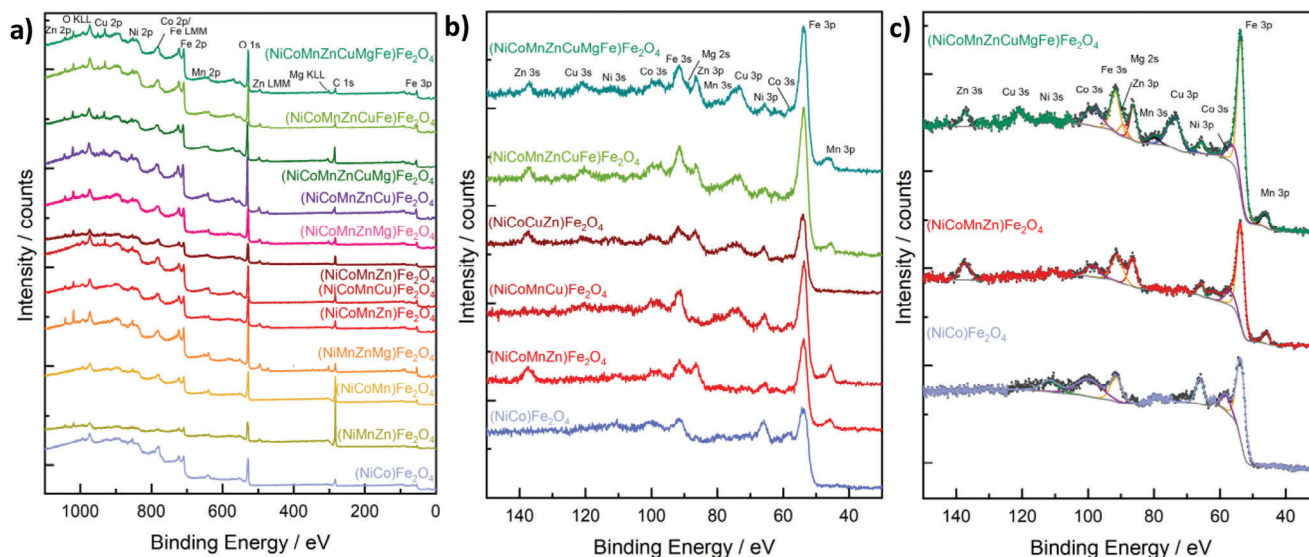


Figure 4. a) XPS survey scans of medium- and high-entropy ferrites, b) high resolution survey scans of the lower binding energy region used for quantification, and c) exemplary fit of such spectra.

which is especially relevant for Ni, Mn, Co, Fe, and Cu, since they can occur in multiple oxidation states. Unfortunately, due to the interference of Auger lines and low signal to noise ratios, a quantification of redox species in compositions containing several 3d transition metals is not possible. However, high-resolution measurements of the Fe 2p signal for several ternary ferrites and (NiCoMnCuZnMg)Fe₂O₄ are highly similar and can be fitted with the constraints for Fe₃O₄ (Fe³⁺ contribution) proposed by Biesinger et al. (Figure S15, Supporting Information), supporting the 3+ oxidation state of Fe.^[62] Small differences in the peak shape between samples can be expected due to differences in the degree of inversion and different Auger contributions.^[63,64] Additionally, the presence of the Co L₃M₄₅M₄₅ line at 713 eV is clearly visible especially for (NiCo)Fe₂O₄.

For Ni, high-resolution spectra of the Ni 2p signal of the binary oxides (NiCo)Fe₂O₄ and (NiZn)Fe₂O₄ were measured in a comparison to that of (NiCoMnCuZnMg)Fe₂O₄. All spectra are highly comparable and strongly resemble that reported for NiFe₂O₄. An exemplary fit of the Ni 2p_{3/2} peak of (NiZn)Fe₂O₄, with the multiplet splitting reported by Biesinger et al. can be found in Figure S15 (Supporting Information).^[62] Therefore, Ni predominantly occurs in the oxidation state of +2 also in the presence of various additional M²⁺ ions. For Cu on the other hand, a partial reduction to Cu⁺ and Cu⁰ was observed, in agreement to literature observations of Cu being prone to reduction when alcohols are used as a solvent.^[53,48] For Mn, the Mn 2p_{3/2} spectra for (MnMg)Fe₂O₄ and (MnZn)Fe₂O₄ allow for a reasonably good fit with the multiplet parameters from Biesinger et al. for MnO.^[62] Small amounts of a reduced manganese species appear to be present in (MnZn)Fe₂O₄. The Mn 2p peak shape of (NiCoMnCuZnMg)Fe₂O₄ is generally similar, however, a strong Ni LMM and Cu LMM peak prevent accurate fitting. For Co the spectral overlap with the Fe LMM signal was too strong to allow for a meaningful fit. The Zn 2p_{3/2} spectrum of (NiCoMnCuZnMg)Fe₂O₄ is again highly similar to that of the binary ferrites. A slight shift toward lower binding energy is ob-

served compared to (MnZn)Fe₂O₄ and (NiZn)Fe₂O₄. The same can be said about (NiZn)Fe₂O₄, albeit to a slightly lesser extent. The modified Auger parameter of (MnZn)Fe₂O₄, (NiZn)Fe₂O₄, and (NiCoMnCuZnMg)Fe₂O₄ are with 2010.2–2010.4 eV slightly higher than that of (ZnMg)Fe₂O₄ of 2009.9 eV, but still in good agreement to literature values for Zn²⁺.^[65] Reasons for the slight peak shifts might be the possible presence of low amounts of a reduced Zn species, or differences in the degree of inversion, since electrons in Zn²⁺ in tetrahedral and octahedral environment might have slightly different binding energies.^[63] From these analyses, it can be inferred that the oxidation state in the high-entropy spinel ferrites is very similar to the oxidation state in binary ferrites and thus not significantly influenced by the mixing with other M²⁺-ions. Some of the employed M²⁺-ions (especially Cu) in the structure might occur in a slightly reduced state, however, all ions are mostly in the target oxidation state also employed in the metal precursor.

Since SEM with EDX only gives insights into the element distribution over a larger area and XPS is a surface sensitive technique, the homogenous distribution of all employed elements in the structure was verified with high-angle annular dark-field scanning transmission electron microscopy (HAADF-STEM) analysis of (NiCoMnCuZnMg)Fe₂O₄ (Figure 5). The crystallization in a spinel structure was confirmed. Additionally, all elements are present in each single particle, proving that they are truly incorporated into the structure. The observed element ratios are with 61.5:23.9:0.9:1.5:2.3:2.1:5.5:2.3 for O:Fe:Mg:Mn:Co:Ni:Cu:Zn in very good agreement to the results obtained from EDX and XPS, further elucidating homogeneity on a nanometre scale as well as across multiple particles. The amount of copper is slightly overestimated, due to EDX signals originating from Cu parts of the STEM holder. The same homogeneity was observed if the mapping was performed over more particles together (Figure S16, Supporting Information). Having exemplified the homogeneous elemental distribution in (NiCoMnCuZnMg)Fe₂O₄, we further demonstrated the

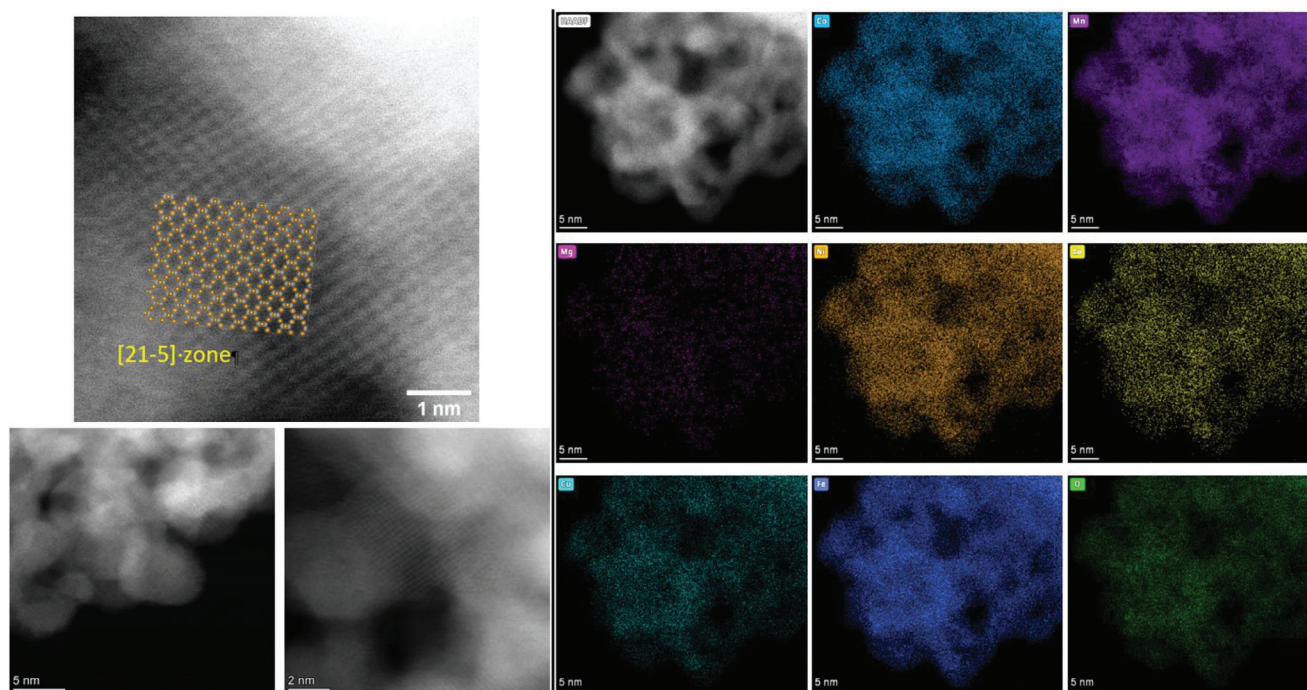


Figure 5. HAADF-STEM of $(\text{NiCoMnCuZnMg})\text{Fe}_2\text{O}_4$ together with EDX, highlighting the homogeneous distribution of elements on the nanometre scale across multiple nanoparticles. The corresponding EDX spectrum is shown in Figure S16 (Supporting Information).

homogeneity in $(\text{NiCoMnCuZn})\text{Fe}_2\text{O}_4$ (Figure S17, Supporting Information) with five M^{2+} -ions and $(\text{NiMnZnMg})\text{Fe}_2\text{O}_4$ containing four M^{2+} -ions (Figure S18, Supporting Information).

After having established phase-purity of the synthesized oxides, we took a closer look at their properties, especially with regards to structure-property relationships. Rietveld refinement of the Ag-XRD patterns was performed in order to gain insights into influences of the elemental composition on crystallite size, lattice parameter/ cell volume and the presence of micro-strain. While the first one is expected to influence the surface area and the number of active catalytic sites, the latter two affect the electronic properties. Especially strain is a factor commonly observed in high-entropy alloys,^[66,3] but also reported for metal chalcogenides.^[26,21] In mixed transition metal high-entropy spinel oxides it was observed that the lattice parameters decreased upon replacement of either Ni or Co by Zn, due to the weaker electronegativity.^[6]

First, crystallite sizes were determined from the (400) reflection in Cu- and Ag-XRD patterns by the integral breadth method, that is, by evaluating the height of a reflection in relation to its area. Thus, a first impression of crystallite sizes could be gained. Due to the broadness of the reflections, only the (400) reflection was used for the first size approximation. The determined sizes from both patterns for each composition were in good agreement, with the one derived from the Ag-XRD pattern being slightly smaller, due to pronounced asymmetry in the reflections that stem from the measurement configuration, in addition to a lower signal to noise ratio in the Cu-XRD patterns. Instrument broadening was not subtracted for this first estimation of crystallite sizes. For all synthesized spinel oxides, the determined crystallite sizes from Cu-XRD patterns are ≈ 6 nm for

as-synthesized and ≈ 7 nm for calcined spinel oxides. From Ag-XRD patterns, the calculated sizes are ≈ 5 nm for as-synthesized and ≈ 6 nm for calcined spinel oxides (Figure S19, Supporting Information). Crystallite sizes determined by Rietveld refinement are in generally good agreement to those calculated with the integral breadth method (Figure 6). Apart from MgFe_2O_4 , which is mostly amorphous directly after the synthesis and still not very crystalline after calcination at 400°C , all binary spinel oxides have similar crystallite sizes of ≈ 6 to 7 nm. Especially for the as-synthesized samples, spinels with more than one M^{2+} -ion have slightly lower crystallite sizes of ≈ 5 nm. There is, however, also a noticeable dependence of the size on the composition. While spinels that do not contain Cu show an almost constant decrease with the number of different M^{2+} -ions, the crystallite sizes of those spinels with Cu are generally larger, probably due to local heating upon microwave absorption and partial reduction of Cu. As-synthesized spinel oxides with high relative amounts of nickel are also smaller, in agreement to the small-crystallite size of NiFe_2O_4 directly after the synthesis (Figure 6b). From a comparison with SEM and STEM images, it can be inferred that the nanoparticles are mostly single-crystalline. No significant difference in the fitted strain is observed, although a slight increase from spinels with four different M^{2+} -ions to seven M^{2+} -ions is observable (Figure S20, Supporting Information).

The lattice parameter is ≈ 8.4 Å for all ferrites (Figure 6). It slightly decreases upon calcination, possibly due to cation redistribution toward a thermodynamically more favored structure, as observed in Raman measurements, in addition to a further condensation of the structural network, and increase in the crystallinity. Furthermore, re-oxidation of partially reduced species might play a part. The determined lattice parameters for ferrites

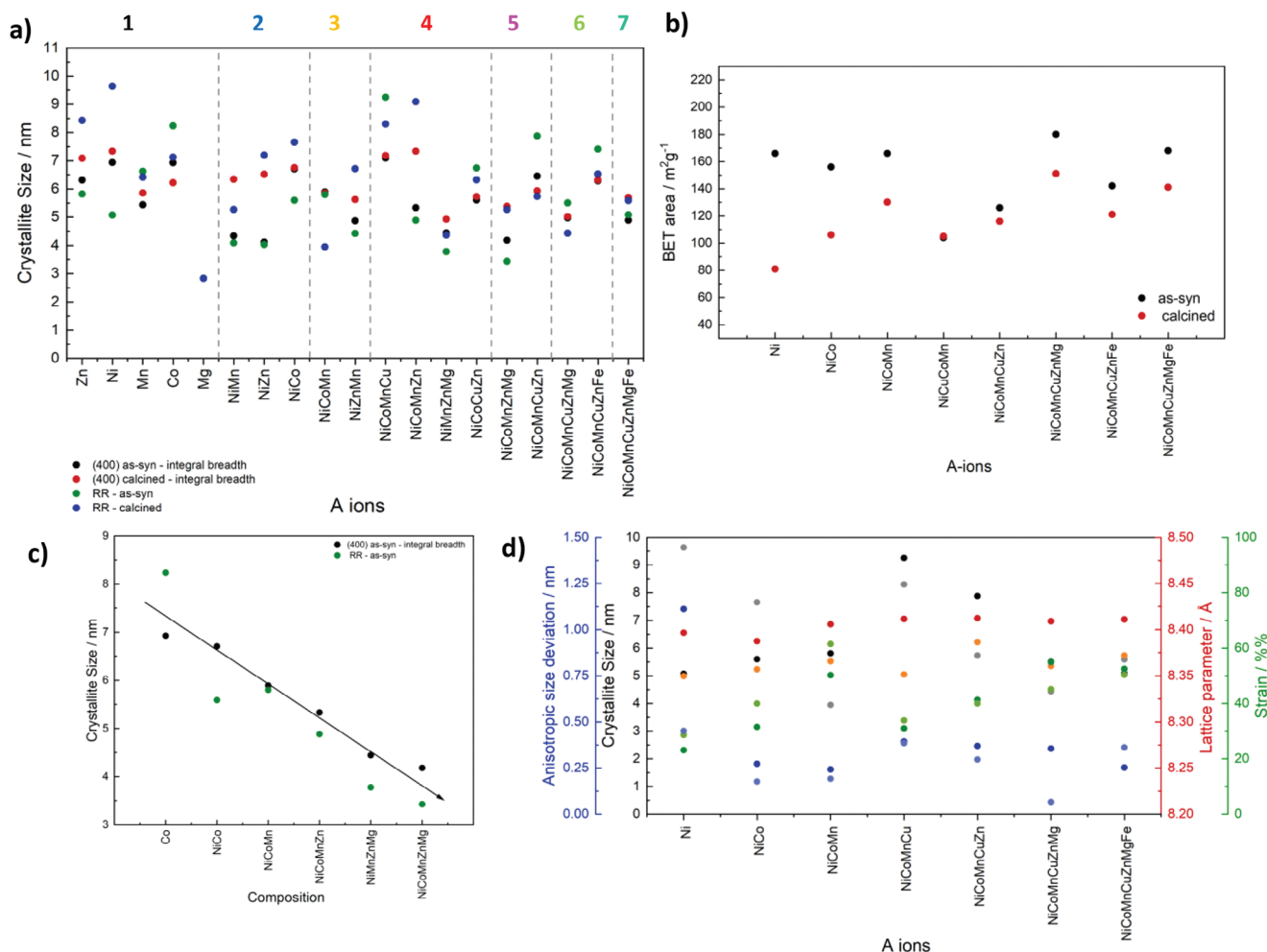


Figure 6. a) Crystallite size depending on the composition determined by the integral breadth method and Rietveld refinement from Ag-XRD patterns, b) BET surface area of selected medium- and high-entropy ferrites, c) crystallite size and composition for selected samples showing the general decrease in crystallite size of compositionally related ferrites with a larger number of M²⁺-ions in the structure, and d) refined parameters for selected samples depending on the composition. As-synthesized samples are depicted in a darker color, whereas calcined ones are shown in paler color.

containing only one M²⁺-ion fit well to literature reports (compare ICDD reference files employed for phase identification). The trend in determined lattice parameters moreover follows the trend in ionic radii, with the values for sixfold coordination reported by Shannon used for the correlation (Figure S21, Supporting Information).^[67] For ternary and quaternary ferrites, those containing more Zn and/ or Mn possess a larger lattice parameter, in agreement to the larger ionic radius, whereas those containing more Co and Ni possess smaller lattice parameters. A decrease in the lattice parameter has also been observed by Jadhav et al. upon Zn substitution by Ni in mixed Zn_xNi_{1-x}Fe₂O₄,^[61] while Ansari et al. reported on an increasing lattice parameter upon Co substitution by Mn.^[68] All in all, the largest lattice parameter is obtained for calcined ZnFe₂O₄, the smallest for calcined MnFe₂O₄ and NiFe₂O₄, with all medium and high entropy spinels having intermediate lattice parameters. This is reflected by a convergence of the maximum of the main reflection (311) ≈12.62° 2θ for high-entropy spinel ferrites (Figure S23, Supporting Information). The fits are depicted in Figures S22–S25 (Supporting Information).

In agreement to the highly similar crystallite size, with a small reduction in size upon the addition of a multitude of different ions, the BET surface area is highly similar for all spinel ferrites of different compositions (Figure 6; Figure S26 and Table S3, Supporting Information). Interestingly, the BET surface area decreases almost consistently for all spinel ferrites upon calcination at 400 °C, although the crystallite size decreases in some cases. The BET area is, however, also influenced by the organic residues adhering to the particle surface. Those amounts are often non-negligible, as observed by XPS and DRIFT analysis and significantly reduced upon calcination (Figure S27, Supporting Information).

The band gap is another important material property that is very sensitive to the composition. Optical absorption in spinels is generally complex, since several transitions might occur, such as ligand to metal charge transfer (LMCT), intersublattice charge transfer (ISCT) between ions at octahedral and tetrahedral sites, intervalent charge transfer (IVCT) between M²⁺ and Fe³⁺ and crystal field (CF) transitions between d-orbitals of one type of ion at the same site.^[34,69] For the latter, relatively small excitation

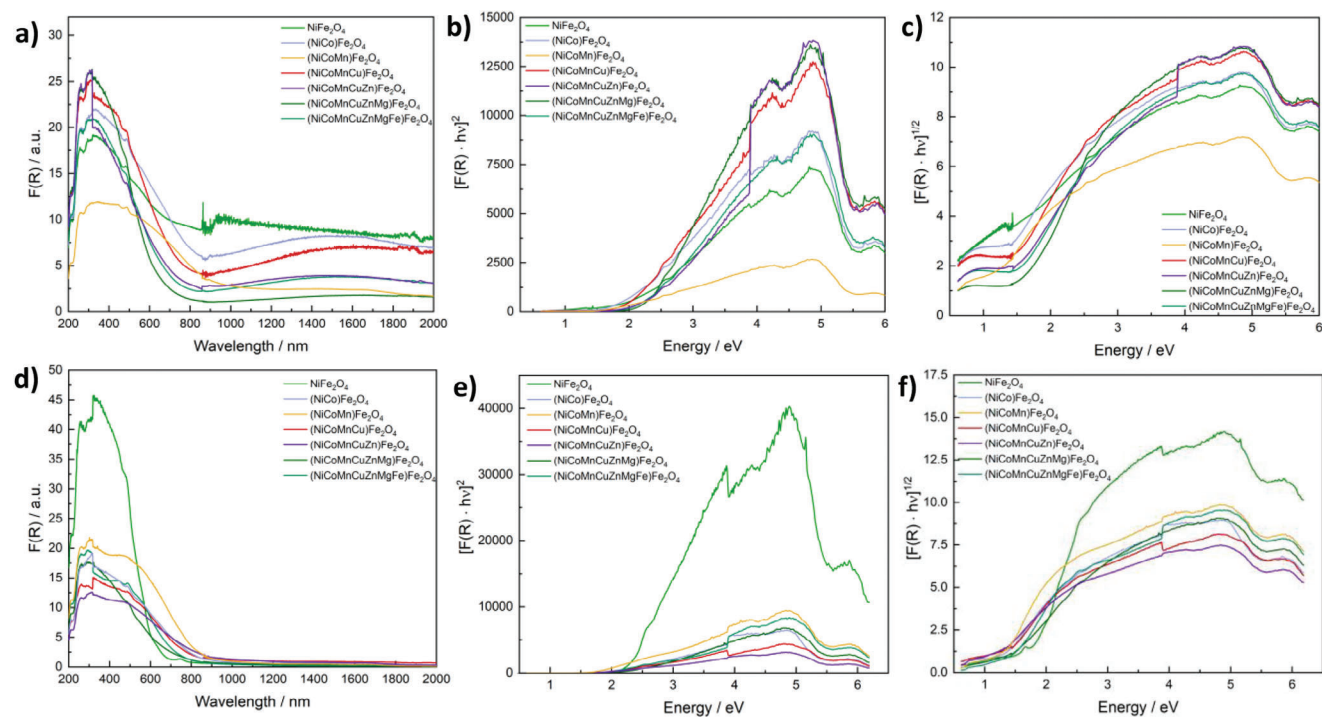


Figure 7. a) Kubelka–Munk plots, b) direct Tauc plots and c) indirect Tauc plots of as-synthesized spinel ferrites (top) and d) Kubelka–Munk, e) direct Tauc and f) indirect Tauc plots for calcined ones (bottom). Sharp features at 319 nm (3.9 eV) result from a measurement artefact of the used spectrometer.

energies are sufficient. Therefore, CF transitions commonly occur in the NIR range, whereas the other three types of optical transitions fall into the UV and visible light range. The main absorption feature can be ascribed to LMCT transitions in normal spinels, while for inverse spinels ISCT and IVCT additionally occur. Absorption features between 2 and 3 eV and those above thus commonly involve mixtures of LMCT, ISCT, and IVCT, the character and ratio of those depends on the M^{2+} -ion.^[69]

While these are local optical transitions that do not necessarily represent classic band gap transitions, attempts have also been made to attribute the observed optical transitions to electronic ones in $NiFe_2O_4$ and $CoFe_2O_4$.^[70–72] In this case, the indirect band gap transition below 2 eV (correlated to an absorption feature at ≈ 2.3 eV) is ascribed to excitation in the minority spin channel, whereas the optical band gaps at 2.29 and 2.77 eV in $NiFe_2O_4$ are ascribed to transitions in both minority and majority channels.^[70,73] The observed spectra are likely a combination between localized optical transitions and fundamental conduction to valence band transitions.

Many of the examined ferrites exhibit an optical absorption feature at ≈ 2.5 eV (Figure 7; Figures S28–S30, Supporting Information), which corresponds to Fe-based ISCT from Fe^{3+} in T_d to Fe^{3+} in O_h sites, or to M^{2+} to Fe^{3+} IVCT in inverse spinels. Whether the M^{2+} (O_h) to Fe^{3+} (O_h) IVCT transition, or the Fe^{3+} (T_d), Fe^{3+} (O_h) ISCT is of lower energy, depends on the M^{2+} cation.^[73] For normal spinels LMCT to Fe^{3+} in O_h sites can occur in this energy range.^[74] For the binary spinel ferrites absorption in this range is the weakest for $ZnFe_2O_4$, in agreement to the mostly normal structure that prevents IVCT and ISCT involving either Fe^{3+} in T_d , or M^{2+} in O_h configuration (Figure 7). A second ISCT transition from Fe^{3+} (T_d) to Fe^{3+} (O_h) appears above 3 eV. The two

separate bands are due to crystal field splitting of Fe 3d orbitals and transitions into t_{2g} and e_g orbitals, respectively, and show a characteristic separation of ≈ 1.4 eV.^[73,69] The features below 1 eV and at ≈ 2.5 eV are most prominent in the indirect Tauc plot and thus correspond to indirect transitions, while the one between 3.7 and 4 eV is most dominant in the direct Tauc plot, in agreement to literature.^[70,71] The possibility of IVCT at octahedral sites for inverted spinels is probably the reason for the larger apparent direct optical band gap of $ZnFe_2O_4$. Specifically, the direct band gap decreases from 2.9 eV in $ZnFe_2O_4$ and 2.4 eV in $MgFe_2O_4$ to 2.0–2.1 eV in the other three binary ferrites (Figure S30, Supporting Information). Since Mg^{2+} does not possess 3d electrons, d-d transitions are weakened compared to ferrites with Mn^{2+} , Ni^{2+} , or Co^{2+} . Indirect band gaps likewise decrease from 2.1 eV in $ZnFe_2O_4$ over 1.6 eV in $MgFe_2O_4$ to around or below 1 eV in the others. The contribution of Zn in ternary and multinary ferrites shows in larger direct and indirect band gaps in those ferrites containing larger amounts of Zn, e.g. $(NiZn)Fe_2O_4$, or $(ZnMg)Fe_2O_4$, in comparison to the others, which is in agreement to reports on $(Ni_xZn_{1-x})Fe_2O_4$.^[61]

The d-d transitions below 1.4 eV (1000 nm) are much more pronounced in the as-synthesized samples compared to the calcined ones, possibly due to more Fe^{3+} with five unpaired d-electrons in octahedral sites (lower degree of inversion). Additionally, symmetry distortions might be healed to some extent during calcination, which would result in less d-d transitions being possible, since they are normally Laporte forbidden. The same effect is observed in medium and high-entropy ferrites (Figure 7).

The band gap values derived from Kubelka–Munk plots decrease slightly upon calcination for some of the ferrites, while for others a slight increase is observed (Figure 8; Table S4,

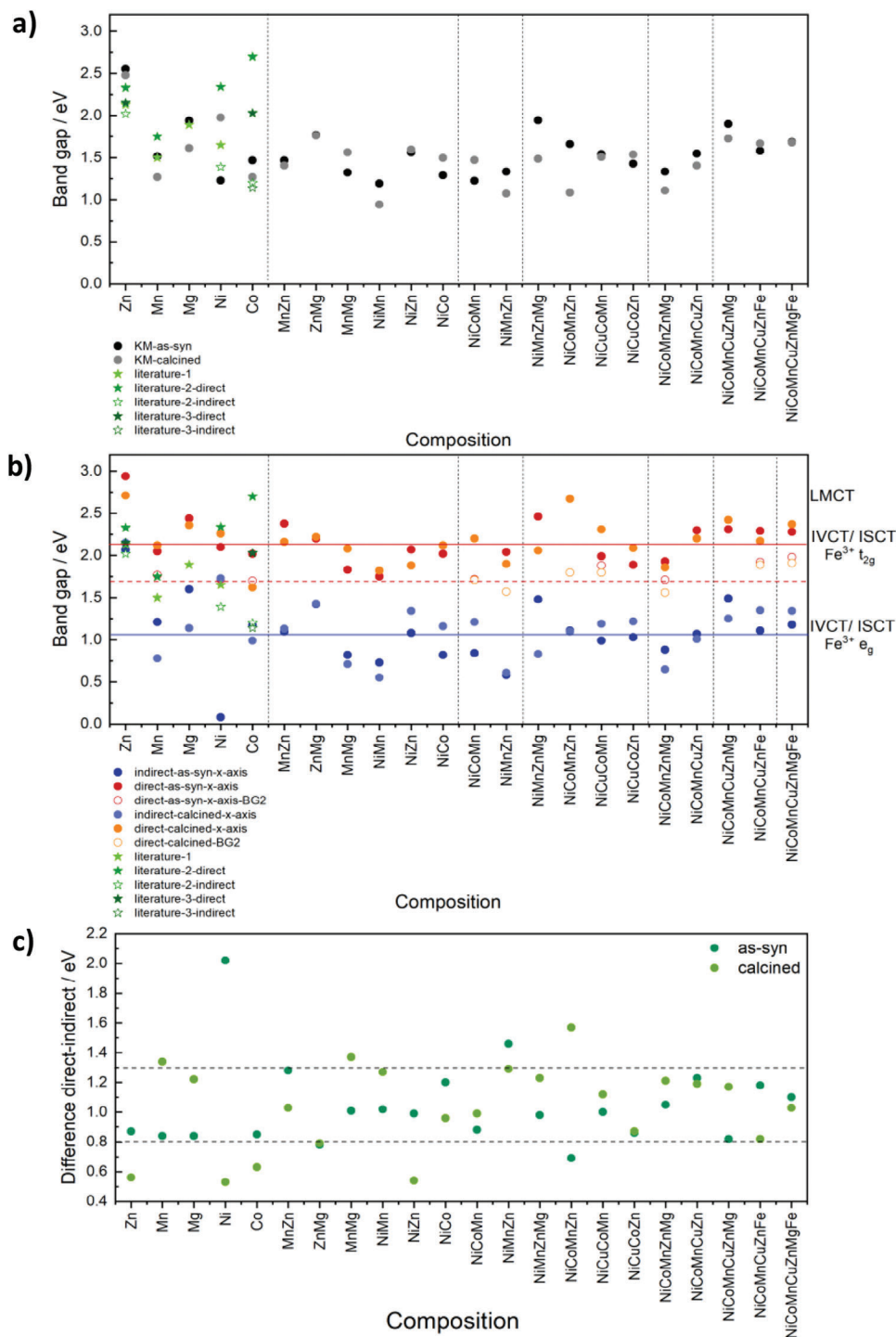


Figure 8. a) Bandgap values derived from Kubelka–Munk plots, b) from direct and indirect Tauc plots and c) the difference between the bandgap values determined from direct and indirect Tauc plots.

Supporting Information). A generally good agreement with literature is observed for binary ferrites.^[51,34,70,71,54,75–77] On the one hand, an increasing crystallinity has an effect, as especially apparent in the spectra of NiFe₂O₄. On the other hand, cation redistribution during calcination might affect the relative intensity of the CT-bands. The differences in apparent band gaps of as-

synthesized and calcined samples are very small in all cases. For those ferrites with strong *d*-transitions in the form of ISCT and IVCT, mostly the transition at ≈ 2.5 eV (overlapping with LMCT transitions) determines the apparent band edge, while for others, such as ZnFe₂O₄, the main contribution arises from LMCT, resulting in the significant difference in the optical band gap.

All medium- and high-entropy ferrites show strong contributions from *d-d* transitions, especially after calcination, which dominate the UV/vis spectra. They do not necessarily represent electronic transitions from valence to conduction band, though.

The difference between the direct band gap at ≈ 2.2 eV and the indirect band gap at ≈ 1 eV is with 1.1–1.2 eV (Figure 8) slightly lower, but still close to the expected 1.3 eV for crystal field splitting in $\text{Fe}^{3+} \text{O}_h$.^[73] This confirms that *d-d* charge transfer transitions dominate the optical properties of the simple and the high-entropy ferrites. The low energy of CF transitions in all ferrites is the reason for the dark brown to black color of the nanoparticulate powders. The deviation from 1.3 eV is probably due to an overlap between ISCT and IVCT and depends on the cations. Since Fe^{3+} is predominant, variations are mainly caused by the different M^{2+} -ions.

NiFe_2O_4 and CoFe_2O_4 are both very efficient earth-abundant electrocatalysts for the OER.^[41,42,45,46] Both are very similar in structure, but vary in regard to the M^{2+} -ion. In order to explore the influence of the nature and diversity of the M^{2+} -ions, the OER performance of various high-entropy ferrites was tested and compared to that of NiFe_2O_4 and CoFe_2O_4 (Figure 9). When combining Co and Ni as M^{2+} -ions, the activity could be significantly improved and the overpotential decreased, especially at higher currents (Table S5, Supporting Information), in agreement to the findings of Chakrapani et al. for Ni-substituted CoFe_2O_4 ,^[78] but in contradiction to Maruthapandian et al. for Co-substituted NiFe_2O_4 .^[79] An improved conductivity has been reported for mixed Co-Ni ferrites, that might contribute to the improved OER activity.^[80] The combination of two different M^{2+} -ions can thus already improve the activity of some highly promising earth abundant electrocatalysts for the OER.

The addition of further M^{2+} -ions, however, resulted in a decreased activity. This can be attributed to low concentrations of the actually active elements, especially Co and Ni. When comparing the binary ferrites, NiFe_2O_4 and CoFe_2O_4 are the only ones exhibiting good OER activity (Figure S31, Supporting Information), whereas the other ferrites are mostly inactive. Especially Ni seems to play a crucial role in the OER activity, since $(\text{NiZn})\text{Fe}_2\text{O}_4$ is still very active, although less so than NiFe_2O_4 and CoFe_2O_4 . Since only the M^{2+} -ion is varied, the relative ratio of Ni or Co in the spinel is with 33% (based on the total metal content) already comparably low. A further replacement by inactive elements leads to a decreased activity, since $(\text{NiCoMn})\text{Fe}_2\text{O}_4$ (40% Ni+Co) is considerably more active than $(\text{NiZnMn})\text{Fe}_2\text{O}_4$ (20% Ni+Co) (Figure 9; Figure S32, Supporting Information). The same trend is observed for the ferrites with four different M^{2+} -ions (Figure 9). Reducing the content of Ni and Co further in the ferrites containing five and more different M^{2+} -ions, leads to a further decrease in the activity. Noticeably, the high-entropy ferrites with six and seven M^{2+} -ions exhibit a slightly improved performance again, although the concentration of Ni and Co are reduced even further. Still, such entropy effects are insufficient to match the high-activity of ferrites with a higher ratio of Ni and Co. Our results show that the OER activity is more dependent on the M^{2+} -ion species than of the number of different ions.

The OER activity was tested for both as-synthesized and calcined spinel ferrites. Interestingly, the as-synthesized spinels ex-

hibit a higher activity compared to the calcined ones, which is in contrast to previous experiments with NiFe_2O_4 ,^[42] but demonstrates that no calcination is required in order to obtain active electrocatalysts, which reduces the energy requirement for the synthesis significantly. The higher activity in as-synthesized ferrites might on the one hand be an effect of the small particle size and the presence of organic residues, both of which improve the dispersibility and ink homogeneity. Furthermore changes in the coordination environment of active elements might influence the performance. The lower activity compared to literature results are likely due to the employed carbon paper electrode, which resulted in lower currents, compared to glassy carbon, or nickel foam (Figure S31, Supporting Information). However, the carbon paper has the advantage of not being active in the OER, in contrast to Ni-foam, which was found to be very active, and of the ferrite ink adhering well to the electrode substrate – much better compared to glassy carbon. A decrease in the performance was still observed with increasing linear sweep voltammetry (LSV) scan number (Figure S31, Supporting Information), which is likely due to a gradual removal of organic residues, but to some extent perhaps also due to powder detachment. It is also apparent for the high-entropy ferrites (Figure S32, Supporting Information) which initially show a better performance. The relative activity depending on the composition, remains, however, the same.

To test the hypothesis of too little concentration of active elements in the high-entropy spinel oxides, four additional ferrites were synthesized, in which half of the Fe^{3+} was replaced by Co^{3+} . Some Cu-by-phases were present in $(\text{NiCoCuZn})_1\text{Fe}_1\text{Co}_1\text{O}_4$ and $(\text{NiCoMnCuZnMg})_1\text{Fe}_1\text{Co}_1\text{O}_4$ directly after the synthesis, which disappeared after calcination (Figure S33, Supporting Information). The activity was significantly improved, compared to the ferrites, with $(\text{NiCoMnCu})_1\text{Fe}_1\text{Co}_1\text{O}_4$ easily outperforming both NiFe_2O_4 and CoFe_2O_4 . A low overpotential of 0.46 V was realized for this spinel at 10 mA. When Cu was replaced by inactive Zn, the activity was significantly reduced. This effect is even more pronounced, when Mg is additionally used. Electron energy loss spectroscopy (EELS) confirmed the oxidation state of Fe^{3+} after partial replacement by Co in $(\text{NiCoMnCu})_1\text{Fe}_1\text{Co}_1\text{O}_4$ (Figure S34, Supporting Information). Interestingly, a comparison with the Fe L-edge in Fe_3O_4 and Fe_2O_3 revealed that in both as-synthesized CoFe_2O_4 and $(\text{NiCoMnCu})\text{Fe}_1\text{Co}_1\text{O}_4$, a low amount of the iron ions (<20%) occur as Fe^{2+} .^[81] This is likely due to redox reactions that are known to occur under the employed conditions, that is, heating in the presence of an oxidizable solvent.^[53] Additionally, the presence of Co in a more oxidized state was verified by a shift of the Co L_3 -edge toward a higher loss energy.^[82]

As these $\text{AFe}_1\text{Co}_1\text{O}_4$ spinel oxides increase the Co content by 33%, they clearly elucidate the reason for the improved OER performance. In addition, the presence of Co^{3+} can significantly improve the performance also compared to CoFe_2O_4 , where Co occurs as Co^{2+} . Therefore, for high-entropy spinels, higher OER activity can be achieved at the price of more Co and Ni contents – and thus also higher material costs, lower sustainability, and abundance. The Fe content in these spinels (67% in AFe_2O_4 , 33% in $\text{AFe}_1\text{Co}_1\text{O}_4$) is still higher than those employed in literature with equimolar ratios of all cations (20% in $(\text{MnFeNiMgCr})_3\text{O}_4$), for which an improved OER activity was reported.^[55]

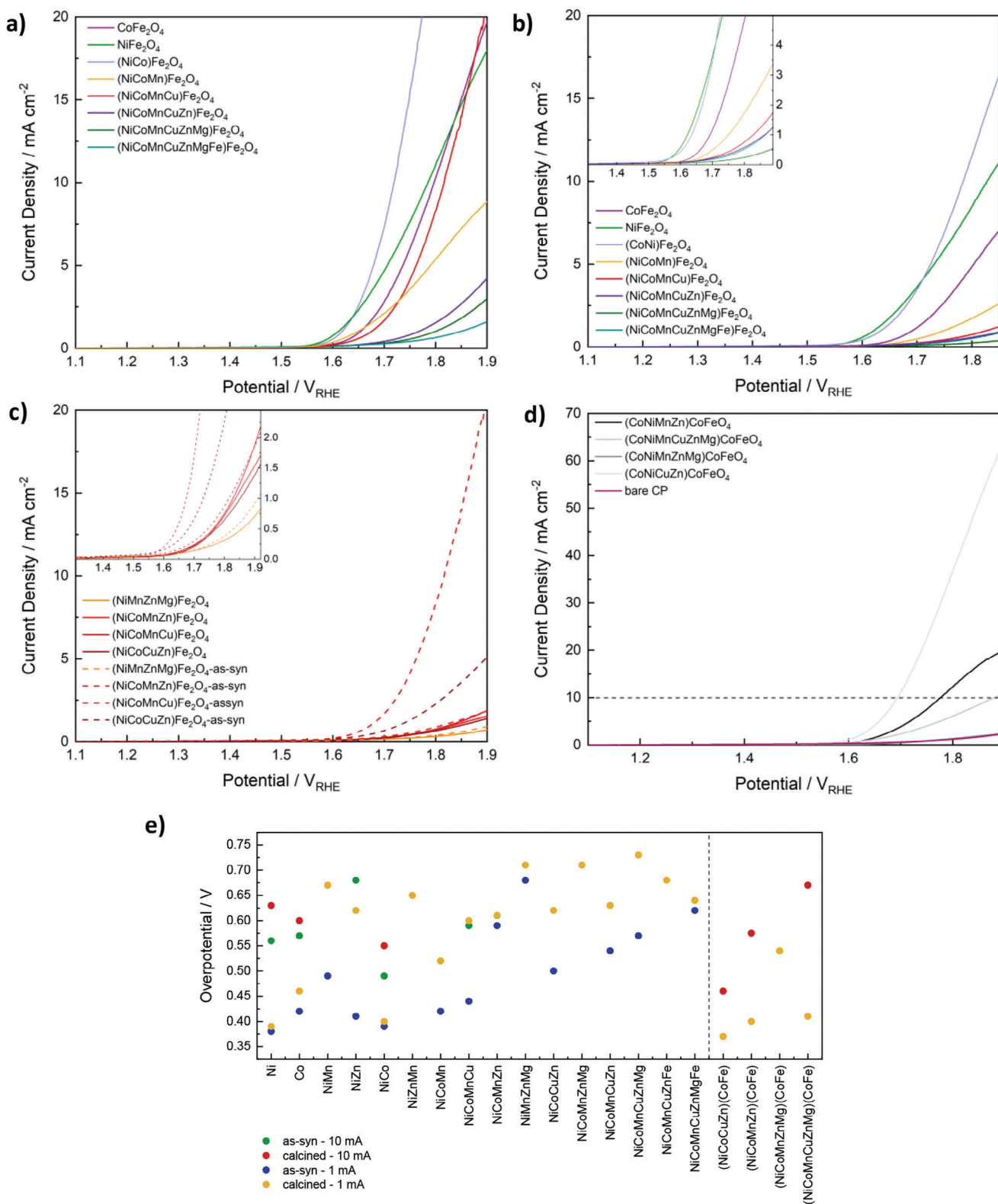


Figure 9. LSV measurements for medium and high-entropy ferrites in comparison to NiFe₂O₄ and CoFe₂O₄, both a) as-syn and b) after calcination. c) LSV scans for ferrites with four different M²⁺-ions are shown in (c), with both the initial sweep (after three previous cyclic voltammetry scans) and the final sweep shown. LSV scans for spinel oxides with Co as a partial replacement for Fe are depicted in (d). A comparison of the determined overpotential at 10 mA (if applicable) and at 1 mA depending on the composition is shown in (e).

3. Conclusion

High-entropy spinel ferrites with a large variety of different M^{2+} -ions were successfully synthesized. A synthesis temperature of 225 °C and a time of 30 min in the microwave was sufficient for the preparation of phase pure high-entropy spinel oxides. These conditions are significantly milder compared to others reported in the literature. Additionally, the large variety of different ferrites synthesized elucidates the versatility of this approach. Due to the low relative ratio of active elements, such as Co and Ni in the structure, the high-entropy spinel ferrites (MFe_2O_4) were less active compared to $NiFe_2O_4$ or $CoFe_2O_4$ in the OER. The most active ferrite was found to be $(NiCo)Fe_2O_4$, which is thus a highly promising earth-abundant OER electrocatalyst. Partial replacement of Fe^{3+} by Co^{3+} resulted in a significantly improved activity exceeding that of either $NiFe_2O_4$ or $CoFe_2O_4$. This result not only proves that the synthesis allows for further variations also on the M^{3+} -ion site, but also paves the way for the design and synthesis of highly active novel high-entropy spinel oxide electrocatalysts under mild conditions.

4. Experimental Section

Synthesis: For the synthesis of 0.5 mmol of AFe_2O_4 , 353.2 mg (1 mmol) of $Fe(acac)_3$ (*Acros Organics*) was dissolved in 15 mL of rac-1-phenylethanol (Sigma-Aldrich) together with equal molar ratios of $M(acac)_2$, with the sum of all $M(acac)_2$ equalling to 0.5 mmol. The solution was transferred to a 30 mL borosilicate microwave vial and either heated as fast as possible – or, if high amounts of $Cu(acac)_2$ were employed, with reduced power – to 225 °C under stirring in a microwave reactor (Anton Paar Monowave 400) equipped with a MAS24 autosampler. The solution was kept at the target temperature for 30 min, before being cooled as fast as possible to 55 °C, using compressed air. The obtained product was precipitated with *n*-pentane and subsequently washed thrice with acetone/water and once with diethyl ether, before finally being dried at 80 °C overnight. A portion of the as-synthesized product was further calcined at 400 °C for 5 h in air (Nabertherm furnace) to improve crystallinity and remove organic residues.

Characterization: Powder XRD was performed on a Malvern PANalytical Empyrean diffractometer, using $Cu K\alpha$ irradiation. A spinning sample holder in Bragg-Brentano geometry was used. Additionally, selected samples were measured on a STOE STADI P Mythen2.4 K diffractometer, using $Ag K\alpha$ irradiation and Hilgenberg capillaries (0.5 mm outer diameter). The instrument was equipped with a $Ge(111)$ monochromator and four Decris MYTHEN2 R 1 K strip detectors.^[83] Rietveld refinements were performed using FullProf.^[84] A Thompson-Cox-Hastings pseudo-Voigt function was used for peak shape modeling.^[85] Refinements were based on the structure reported by Mahmood et al. for cubic $CuFe_2O_4$, changing the A ion to either Co, Ni, or Mn, as appropriate and calculated absorption correction for $NiFe_2O_4$.^[86] For ferrites containing only one A-ion, lattice parameters in the starting conditions and absorption correction were adapted. Refined parameters include instrumental zero shift, background, FWHM parameters, mainly U and Y, lattice parameters, isotropic B, scale, source width/detector distance, size anisotropy (spherical harmonics) and, if required, asymmetry parameters. Occupation refinement was only attempted for structures with one A-ion. Instrumental broadening was determined with LaB_6 (NIST SRM 660c) as a standard. Size was calculated by FullProf from the size parameters contributing to the FWHM, that is, IG for the Gaussian contribution, as well as Y and Sz for the Lorentzian contribution. Strain was calculated from the strain parameters, that is, mainly U for the Gaussian contribution and X for the Lorentzian contribution.

UV/vis/NIR spectra were obtained on a Perkin Elmer Lambda 750 spectrometer, equipped with a Praying Mantis (Harrick) and using spectralon

as a white standard. DRIFT (Diffuse Reflectance Infrared Fourier Transformed) spectra were measured on a Bruker Alpha II spectrometer. Raman measurements were conducted on a Horiba Yvon Raman microscope, equipped with a 11.5 W He-Ne laser ($\lambda = 633$ nm). The laser intensity was reduced if required to avoid extensive sample heating and undesired interference from fluorescence. Casa XPS 2.3.25 was used for spectra fitting, assuming Gaussian-Lorentzian peak shapes (GL(50)). Nitrogen physisorption measurements were performed on a Quadrasorb Evo and a Nova 800 device from Anton Paar QuantaTec at 77 K. Samples were degassed for 12 h at 120 °C prior to the measurements. The surface area was evaluated with the software ASiQwin using the Brunauer–Emmet–Teller (BET) model. XPS was performed on a VersaProbe III Scanning XPS Microprobe (Physical Electronics PHI), using monochromated $Al K\alpha$ irradiation. Beam voltage and X-ray power were set to 15 kV and 25 W, respectively, and the spot size was 100 μm . Wide-range survey scans were measured with a step size of 0.4 eV, a pass energy of 224 eV and a time per step of 50 ms. High-resolution short-range survey scans and conventional high-resolution spectra were measured with a step size of 0.1 eV, a pass energy of 26 eV and a time per step of 50 ms. Samples were continuously flooded with electrons and Ar^+ ions at low energy. CasaXPS 2.3.25 was used for data evaluation, using Shirley or linear backgrounds and LA(1643) (survey) or GL(30) (high-resolution) line shapes.^[87] Binding energies were corrected using the C 1s (C-C, C-H) peak as reference at 284.8 eV.

SEM and EDX were performed on a Zeiss Leo 1530 device additionally equipped with an ultra-dry EDX detector from Thermo Fisher Scientific NS7. Samples were sputter coated with platinum (Cressington Sputter Coater 208 HR). An acceleration voltage of 3 and 20 kV was used for SEM and EDX, respectively. For the WDX analysis, a Zeiss Ultra plus electron microscope and a Magna Ray WDX-spectrometer from Thermo Fisher Scientific NS7 were used with the acceleration voltage set to 15 kV.

STEM was performed on a Titan Themis microscope operated at 300 kV. Nanoparticle samples were drop cast onto a gold grid with lacey carbon. STEM-EDX spectrum imaging was acquired using a SuperX detector covering 0.7 sr collection angle. STEM-EELS spectrum imaging was collected using a Quantum ERS spectrometer. Multivariate statistical analysis was conducted to denoise the spectrum imaging datasets and detect for potential inhomogeneity in the elemental distribution.^[88]

A three electrode H-cell setup was used for electrochemical measurements. A platinum counter electrode, a reversible hydrogen electrode reference electrode (Gaskatel), a Selemion AMV-N anion-exchange membrane (AGC group) and either a Parstat 3000A-DX potentiostat (Princeton Applied Research) and the software VersaStudios, or a Gamry Reference 3000 potentiostat and the software Gamry Frameworks were used, respectively. iR compensation for measurements with the Parstat potentiostat was done via EIS measurements, while the current interrupt method was used for correction with the Gamry potentiostat. The internal resistance was measured prior to the electrochemical characterizations and was very small. All reported potentials are compensated, if not otherwise noted. 1 M KOH was employed as electrolyte that was continuously purged with Ar . For the preparation of the working electrode, 10 mg of the respective sample were dispersed in 300 μL of *i*-propanol (p.a.) and 20 μL of a 5 wt.% Nafion solution (Alfa Aesar) using ultrasonication. 50 μL of the dispersion were drop-cast onto carbon paper (Freudenberg H2315-C2) with the exposed surface area being restricted to 1 cm^2 using Kapton tape. 25 LSV scans were recorded at a sweep rate of 5 $mV s^{-1}$ after three initial CV scans.

Supporting Information

Supporting Information is available from the Wiley Online Library or from the author.

Acknowledgements

The authors thank Dr. Jana Timm and Jonas Jungmann for nitrogen physisorption measurements, Dr. Anja Hofmann and Mirco Ade for SEM and EDX analysis, and Lion Schumacher for XPS measurements (all university of Bayreuth). Additionally, the authors thank Martina Heider for the

WDX measurements and the Bavarian Polymer institute (BPI) for usage of the XPS and SEM devices (KeyLabs Device Engineering and Electron and Optical Microscopy). J.Z. and R.M. gratefully acknowledge funding in the graduate school of the Bavarian Center for Battery Technology (BayBatt), University of Bayreuth, and by the Bavarian State Ministry of Science, Research and Arts within the scope of Solar Technologies Go Hybrid. N.C. is grateful for financial support from the Alexander von Humboldt Foundation. S.Z. acknowledges funding from the German Research Foundation (DFG) under the framework of the priority program 2370 (Project number: 502202153).

Open access funding enabled and organized by Projekt DEAL.

Conflict of Interest

The authors declare no conflict of interest.

Data Availability Statement

The data that support the findings of this study are available from the corresponding author upon reasonable request.

Keywords

electrocatalysis, high-entropy oxide, nanoparticles, spinel, water oxidation

Received: August 25, 2023

Revised: October 12, 2023

Published online: November 15, 2023

- [1] Z. Jin, J. Lyu, Y.-L. Zhao, H. Li, X. Lin, G. Xie, X. Liu, J.-J. Kai, H.-J. Qiu, *ACS Mater. Lett.* **2020**, *2*, 1698.
- [2] J. W. Yeh, Y. L. Chen, S. J. Lin, S. K. Chen, *Mater. Sci. Forum* **2007**, *560*, 1.
- [3] Q. Ding, Y. Zhang, X. Chen, X. Fu, D. Chen, S. Chen, L. Gu, F. Wei, H. Bei, Y. Gao, M. Wen, J. Li, Z. Zhang, T. Zhu, R. O. Ritchie, Q. Yu, *Nature* **2019**, *574*, 223.
- [4] H. Li, J. Lai, Z. Li, L. Wang, *Adv. Funct. Mater.* **2021**, *31*, 2106715.
- [5] C. M. Rost, E. Sachet, T. Borman, A. Moballegh, E. C. Dickey, D. Hou, J. L. Jones, S. Curtarolo, J.-P. Maria, *Nat. Commun.* **2015**, *6*, 8485.
- [6] A. Mao, H.-Z. Xiang, Z.-G. Zhang, K. Kuramoto, H. Zhang, Y. Jia, *J. Magn. Magn. Mater.* **2020**, *497*, 165884.
- [7] J. Dabrowa, M. Stygar, A. Mikula, A. Knapik, K. Mroczka, W. Tejchman, M. Danielewski, M. Martin, *Mater. Lett.* **2018**, *216*, 32.
- [8] Z. Jin, J. Lyu, Y.-L. Zhao, H. Li, Z. Chen, X. Lin, G. Xie, X. Liu, J.-J. Kai, H.-J. Qiu, *Chem. Mater.* **2021**, *33*, 1771.
- [9] D. Moskovskikh, S. Vorotilo, V. Buinevich, A. Sedegov, K. Kuskov, A. Khort, C. Shuck, M. Zhukovskiy, A. Mukasyan, *Sci. Rep.* **2020**, *10*, 19874.
- [10] L. Wu, X. Shen, Z. Ji, J. Yuan, S. Yang, G. Zhu, L. Chen, L. Kong, H. Zhou, *Adv. Funct. Mater.* **2022**, *33*, 2208170.
- [11] M. Guo, P. Li, A. Wang, J. Wang, J. Chen, F. Lei, P. Hao, X. Sun, J. Xie, B. Tang, *Chem. Commun.* **2023**, *59*, 5098.
- [12] L. Lin, K. Wang, A. Sarkar, C. Njel, G. Karkera, Q. Wang, R. Azmi, M. Fichtner, H. Hahn, S. Schweidler, B. Breitung, *Adv. Energy Mater.* **2022**, *12*, 2103090.
- [13] M. Cui, C. Yang, B. Li, Q. Dong, M. Wu, S. Hwang, H. Xie, X. Wang, G. Wang, L. Hu, *Adv. Energy Mater.* **2021**, *11*, 2002887.
- [14] A. Sarkar, Q. Wang, A. Schiele, M. R. Chellali, S. S. Bhattacharya, D. Wang, T. Brezesinski, H. Hahn, L. Velasco, B. Breitung, *Adv. Mater.* **2019**, *31*, 1806236.
- [15] J. Zhang, J. Yan, S. Calder, Q. Zheng, M. A. Mcguire, D. L. Abernathy, Y. Ren, S. H. Lapidus, K. Page, H. Zheng, J. W. Freeland, J. D. Budai, R. P. Hermann, *Chem. Mater.* **2019**, *31*, 3705.
- [16] T. X. Nguyen, J. Patra, J.-K. Chang, J.-M. Ting, *J. Mater. Chem. A* **2020**, *8*, 18963.
- [17] G. H. J. Johnstone, M. U. González-Rivas, K. M. Taddei, R. Sutarto, G. A. Sawatzky, R. J. Green, M. Oudah, A. M. Hallas, *J. Am. Chem. Soc.* **2022**, *144*, 20590.
- [18] J. Zhang, J. Yan, S. Calder, Q. Zheng, M. A. Mcguire, D. L. Abernathy, Y. Ren, S. H. Lapidus, K. Page, H. Zheng, J. W. Freeland, J. D. Budai, R. P. Hermann, *Chem. Mater.* **2019**, *31*, 3705.
- [19] T. X. Nguyen, Y.-C. Liao, C.-C. Lin, Y.-H. Su, J.-M. Ting, *Adv. Funct. Mater.* **2021**, *31*, 2101632.
- [20] Y. Sharma, B. L. Musico, X. Gao, C. Hua, A. F. May, A. Herklotz, A. Rastogi, D. Mandrus, J. Yan, H. N. Lee, M. F. Chisholm, V. Keppens, T. Z. Ward, *Phys. Rev. Mater.* **2018**, *2*, 060404.
- [21] J. Gild, M. Samiee, J. L. Braun, T. Harrington, H. Vega, P. E. Hopkins, K. Vecchio, J. Luo, *J. Eur. Ceram. Soc.* **2018**, *38*, 3578.
- [22] F. Zhang, F. Cheng, C. Cheng, M. Guo, Y. Liu, Y. Miao, F. Gao, X. Wang, *J. Mater. Sci. Technol.* **2022**, *105*, 122.
- [23] A. Sarkar, B. Breitung, H. Hahn, *Scr. Mater.* **2020**, *187*, 43.
- [24] J.-W. Yeh, S.-K. Chen, S.-J. Lin, J.-Y. Gan, T.-S. Chin, T.-T. Shun, C.-H. Tsau, S.-Y. Chang, *Adv. Eng. Mater.* **2004**, *6*, 299.
- [25] J.-W. Yeh, S.-J. Lin, *J. Mater. Res.* **2018**, *33*, 3129.
- [26] M. A. Buckingham, B. Ward-O'Brien, W. Xiao, Y. Li, J. Qu, D. J. Lewis, *Chem. Commun.* **2022**, *58*, 8025.
- [27] G. Pacchioni, *Nat. Rev. Mater.* **2022**, *7*, 156.
- [28] W.-J. Jiang, T. Tang, Y. Zhang, J.-S. Hu, *Acc. Chem. Res.* **2020**, *53*, 1111.
- [29] M. Fu, X. Ma, K. Zhao, X. Li, D. Su, *iScience* **2021**, *24*, 102177.
- [30] Y. Zhang, W. Dai, P. Zhang, T. Lu, Y. Pan, *J. Alloys Compd.* **2021**, *868*, 159064.
- [31] Y. Gu, A. Bao, X. Wang, Y. Chen, L. Dong, X. Liu, H. Pan, Y. Li, X. Qi, *Nanoscale* **2022**, *14*, 515.
- [32] X. Xu, Z. Shao, S. P. Jiang, *Energy Technol.* **2022**, *10*, 2200573.
- [33] A. Sarkar, L. Velasco, D. Wang, Q. Wang, G. Talasila, L. De Biasi, C. Kübel, T. Brezesinski, S. S. Bhattacharya, H. Hahn, B. Breitung, *Nat. Commun.* **2018**, *9*, 3400.
- [34] K. R. Sanchez-Lievano, J. L. Stair, K. E. Knowles, *Inorg. Chem.* **2021**, *60*, 4291.
- [35] X. Ge, Y. Liu, F. W. T. Goh, T. S. A. Hor, Y. Zong, P. Xiao, Z. Zhang, S. H. Lim, B. Li, X. Wang, Z. Liu, *ACS Appl. Mater. Interfaces* **2014**, *6*, 12684.
- [36] M. Li, Y. Xiong, X. Liu, X. Bo, Y. Zhang, C. Han, L. Guo, *Nanoscale* **2015**, *7*, 8920.
- [37] M. Harada, F. Kotegawa, M. Kuwa, *ACS Appl. Energy Mater.* **2022**, *5*, 278.
- [38] Y. Zhou, Y. Du, S. Xi, Z. J. Xu, *Electrocatalysis* **2018**, *9*, 287.
- [39] X.-T. Wang, T. Ouyang, L. Wang, J.-H. Zhong, Z.-Q. Liu, *Angew. Chemie* **2020**, *132*, 6554.
- [40] X.-M. Liu, X. Cui, K. Dastafkan, H.-F. Wang, C. Tang, C. Zhao, A. Chen, C. He, M. Han, Q. Zhang, *J. Energy Chem.* **2020**, *53*, 290.
- [41] C. Simon, J. Timm, D. Tetzlaff, J. Jungmann, U. P. Apfel, R. Marschall, *ChemElectroChem* **2021**, *8*, 227.
- [42] C. Simon, M. B. Zakaria, H. Kurz, D. Tetzlaff, A. Blösser, M. Weiss, J. Timm, B. Weber, U.-P. Apfel, R. Marschall, *Chem. – A Eur. J.* **2021**, *27*, 16990.
- [43] H. Yang, Y. Liu, S. Luo, Z. Zhao, X. Wang, Y. Luo, Z. Wang, J. Jin, J. Ma, *ACS Catal.* **2017**, *7*, 5557.
- [44] L. S. Ferreira, T. R. Silva, V. D. Silva, R. A. Raimundo, T. A. Simões, F. J. A. Loureiro, D. P. Fagg, M. A. Morales, D. A. Macedo, *Adv. Powder Technol.* **2022**, *33*, 103391.
- [45] V. D. Silva, L. S. Ferreira, T. A. Simões, E. S. Medeiros, D. A. Macedo, *J. Colloid Interface Sci.* **2019**, *540*, 59.
- [46] S. Zhu, J. Lei, Y. Qin, L. Zhang, L. Lu, *RSC Adv.* **2019**, *9*, 13269.

- [47] D. González-Flores, K. Klingan, P. Chernev, S. Loos, M. R. Mohammadi, C. Pasquini, P. Kubella, I. Zaharieva, R. D. L. Smith, H. Dau, *Sustain. Energy Fuels* **2018**, *2*, 1986.
- [48] J. Zander, M. Weiss, R. Marschall, *Adv. Energy Sustain. Res.* **2023**, *4*, 2200184.
- [49] P. Dolcet, K. Kirchberg, A. Antonello, C. Suchomski, R. Marschall, S. Diodati, R. Muñoz-Espí, K. Landfester, S. Gross, *Inorg. Chem. Front.* **2019**, *6*, 1527.
- [50] D. Santos-Carballal, A. Roldan, R. Grau-Crespo, N. H. De Leeuw, *Phys. Rev. B – Condens. Matter Mater. Phys.* **2015**, *91*, 195106.
- [51] A. Bloesser, H. Kurz, J. Timm, F. Wittkamp, C. Simon, S. Hayama, B. Weber, U.-P. Apfel, R. Marschall, *ACS Appl. Nano Mater.* **2020**, *3*, 11587.
- [52] R. Deshmukh, M. Niederberger, *Chem. – A Eur. J.* **2017**, *23*, 8542.
- [53] M. Niederberger, G. Garnweitner, *Chem. – A Eur. J.* **2006**, *12*, 7282.
- [54] C. Simon, A. Blösser, M. Eckardt, H. Kurz, B. Weber, M. Zobel, R. Marschall, *Zeitschrift für Anorg. und Allg. Chemie* **2021**, *647*, 2061.
- [55] Z. Sun, Y. Zhao, C. Sun, Q. Ni, C. Wang, H. Jin, *Chem. Eng. J.* **2022**, *431*, 133448.
- [56] A. Navrotsky, O. J. Kleppa, *J. Inorg. Nucl. Chem.* **1967**, *29*, 2701.
- [57] A. Navrotsky, O. J. Kleppa, *J. Inorg. Nucl. Chem.* **1968**, *30*, 479.
- [58] K. Ugendar, V. Hari Babu, V. Raghavendra Reddy, G. Markaneyulu, *J. Magn. Magn. Mater.* **2019**, *484*, 291.
- [59] M. Shanigaram, U. Kodam, J.-S. Noh, Y.-W. Nam, *J. Phys. Chem. Solids* **2022**, *171*, 111036.
- [60] V. H. Ong, T. N. Pham, V. M. Tien, N. X. Dinh, N. Thi Lan, N. Van Quy, T. N. Bach, V. D. Lam, L. M. Tung, A.-T. Le, *J. Alloys Compd.* **2023**, *949*, 169880.
- [61] J. Jadhav, S. Biswas, A. K. Yadav, S. N. Jha, D. Bhattacharyya, *J. Alloys Compd.* **2017**, *696*, 28.
- [62] M. C. Biesinger, B. P. Payne, A. P. Grosvenor, L. W. M. Lau, A. R. Gerson, R. S. C. Smart, *Appl. Surf. Sci.* **2011**, *257*, 2717.
- [63] M. Fantauzzi, F. Secci, M. Sanna Angotzi, C. Passiu, C. Cannas, A. Rossi, *RSC Adv.* **2019**, *9*, 19171.
- [64] A. P. Grosvenor, B. A. Kobe, M. C. Biesinger, N. S. Mcintyre, *Surf. Interface Anal.* **2004**, *36*, 1564.
- [65] M. C. Biesinger, L. W. M. Lau, A. R. Gerson, R. S. C. Smart, *Appl. Surf. Sci.* **2010**, *257*, 887.
- [66] M.-H. Tsai, *Entropy* **2013**, *15*, 5338.
- [67] R. D. Shannon, *Acta Crystallogr., Sect. A: Found. Crystallogr.* **1976**, *32*, 751.
- [68] S. M. Ansari, K. C. Ghosh, R. S. Devan, D. Sen, P. U. Sastry, Y. D. Kolekar, C. V. Ramana, *ACS Omega* **2020**, *5*, 19315.
- [69] V. Vziagin, P. Richter, T. Böntgen, M. Lorenz, M. Ziese, D. R. T. Zahn, G. Salvan, M. Grundmann, R. Schmidt-Grund, *Phys. status solidi* **2016**, *253*, 429.
- [70] Q.-C. Sun, H. Sims, D. Mazumdar, J. X. Ma, B. S. Holinsworth, K. R. O'neal, G. Kim, W. H. Butler, A. Gupta, J. L. Musfeldt, *Phys. Rev. B – Condens. Matter Mater. Phys.* **2012**, *86*, 205106.
- [71] K. Dileep, B. Loukya, N. Pachauri, A. Gupta, R. Datta, *J. Appl. Phys.* **2014**, *116*, 103505.
- [72] B. S. Holinsworth, D. Mazumdar, H. Sims, Q.-C. Sun, M. K. Yurtisigi, S. K. Sarker, A. Gupta, W. H. Butler, J. L. Musfeldt, *Appl. Phys. Lett.* **2013**, *103*, 082406.
- [73] K. J. Kim, H. S. Lee, M. H. Lee, S. H. Lee, *J. Appl. Phys.* **2002**, *91*, 9974.
- [74] K. J. Kim, J. H. Lee, S. H. Lee, *J. Magn. Magn. Mater.* **2004**, *279*, 173.
- [75] O. M. Lemine, M. Bououdina, M. Sajieddine, A. M. Al-Saie, M. Shafi, A. Khatab, M. Al-Hilali, M. Henini, *Phys. B Condens. Matter* **2011**, *406*, 1989.
- [76] M. Bohra, V. Alman, R. Arras, *Nanomaterials* **2021**, *11*, 1286.
- [77] A. Manikandan, J. Judith Vijaya, M. Sundararajan, C. Meganathan, L. J. Kennedy, M. Bououdina, *Superlattices Microstruct.* **2013**, *64*, 118.
- [78] K. Chakrapani, G. Bendt, H. Hajiyani, I. Schwarzrock, T. Lunkenbein, S. Salamon, J. Landers, H. Wende, R. Schlögl, R. Pentcheva, M. Behrens, S. Schulz, *ChemCatChem* **2017**, *9*, 2988.
- [79] V. Maruthapandian, M. Mathankumar, V. Saraswathy, B. Subramanian, S. Muralidharan, *ACS Appl. Mater. Interfaces* **2017**, *9*, 13132.
- [80] I. Shakir, A. Rasheed, S. Haider, M. F. Aly Aboud, *Ceram. Int.* **2019**, *45*, 18099.
- [81] S. Zhang, H. Hajiyani, A. G. Hufnagel, J. Kampmann, B. Breitbach, T. Bein, D. Fattakhova-Rohlfing, R. Pentcheva, C. Scheu, *Zeitschrift für Phys. Chemie* **2020**, *234*, 683.
- [82] Y. Yang, Y. Xiong, M. E. Holtz, X. Feng, R. Zeng, G. Chen, F. J. Disalvo, D. A. Muller, H. C. D. Abrun~A, *Proc. Natl. Acad. Sci. USA* **2019**, *116*, 24425.
- [83] S. L. J. Thomae, N. Prinz, T. Hartmann, M. Teck, S. Correll, M. Zobel, *Rev. Sci. Instrum.* **2019**, *90*, 043905.
- [84] J. Rodríguez-Carvajal, *Phys. B Phys. Condens. Matter* **1993**, *192*, 55.
- [85] P. Thompson, D. E. Cox, J. B. Hastings, *J. Appl. Cryst.* **1987**, *20*, 79.
- [86] N. B. Mahmood, F. R. Saeed, K. R. Gbashi, A. Hamodi, Z. M. Jaffar, *J. Mech. Behav. Mater.* **2021**, *30*, 220.
- [87] N. Fairley, V. Fernandez, M. Richard-Plouet, C. Guillot-Deudon, J. Walton, E. Smith, D. Flahaut, M. Greiner, M. Biesinger, S. Tougaard, D. Morgan, J. Baltrusaitis, *Appl. Surf. Sci. Adv.* **2021**, *5*, 100112.
- [88] S. Zhang, C. Scheu, *Microscopy* **2018**, *67*, i133.